

Performance enhancement of twisted-bladed Savonius vertical axis wind turbines



Ahmed S. Saad^{a,e}, Ibrahim I. El-Sharkawy^{a,c}, Shinichi Ookawara^{a,d}, Mahmoud Ahmed^{a,b,*}

^a Department of Energy Resources Engineering, Egypt-Japan University of Science and Technology, Alexandria 21934, Egypt

^b Mechanical Engineering Department, Assiut University, Assiut 71516, Egypt

^c Mechanical Power Engineering Department, Faculty of Engineering, Mansoura University, Mansoura 35516, Egypt

^d Department of Chemical Science and Engineering, Tokyo Institute of Technology, Tokyo 152-8552, Japan

^e Mechanical Power Engineering Department, Faculty of Engineering, Menoufia University, Menoufia 32511, Egypt

ARTICLE INFO

Keywords:

Twisted Savonius rotor
Performance enhancement
Overlap ratio
End plate
Wind velocity

ABSTRACT

It is important to determine the most optimal configuration of a Savonius vertical axis wind turbine that attains the best performance with a high self-starting ability. Thus, the effects of several design parameters including twist angle, overlap ratio, and endplates size ratio, along with the wind velocity on the performance of the Savonius wind turbine are investigated. Novel assessment methods based on flow field characteristics such as streamlines and pressure fields around the Savonius wind turbine are carried out. This is the first contribution to understand how geometrical variables influence the aerodynamic performance of the twisted Savonius rotor. Moreover, the variation of torque, power, thrust, and static torque coefficients are estimated. Thus, a three-dimensional, incompressible unsteady Reynolds-averaged Navier-Stokes model in conjunction with $k-\omega$ shear-stress transport turbulence model is developed. The model is numerically simulated and validated using the experimental and numerical data available in literature. Results indicate that the Savonius rotor with a twist angle of 45°, an overlapping ratio of zero, and endplates size ratio of 1.1 attains the highest net output power compared to other designs. It is found that at a wind velocity of 6 m/s, the Savonius rotor achieves a maximum power coefficient of 0.223, and with further increase of the wind velocity to 10 m/s, the power coefficient reaches 0.231. In addition, the current developed design has a positive static torque coefficient at all rotor angles, and consequently, it achieves a high self-starting ability. However, for the conventional (untwisted) design, the maximum attainable power coefficient was found to be 0.174 at an overlapping ratio of 0.15, and equal endplate size ratio. In addition, negative values of the static torque coefficient were observed at a specific range of rotor angles that prevent the self-starting ability. Accordingly, the new twisted rotor design not only enhances the power coefficient but the self-starting ability as well. The findings of the current results provide another direction for researchers and designers to utilize the twisted Savonius wind turbine.

1. Introduction

In recent decades, an increase in the human population has led to dramatic growth in energy demand [1]. This has depleted fossil fuels and raised levels of global warming, weather change and green-house gas emissions, which has motivated research in alternative energy sources [2]. Renewable energy and decentralized power generation can be used as alternatives to reduce the exploitation of conventional energy for more sustainable development and to reduce its harmful impact on society. Wind energy is a renewable energy source that is abundant, clean, and cheap [3]. Nowadays, wind energy is established as a mainstream form of energy in electrical power generation. The

global cumulative installed capacity of wind power increased significantly from 24 GW in 2001 to 591 GW in 2018 and is expected to reach 839 GW by 2023 [4].

Wind turbines are broadly classified based on the axis of rotation into two main categories, horizontal axis wind turbines (HAWTs) and vertical axis wind turbines (VAWTs) [5]. Although HAWTs continue to be commercially viable for large-scale power production, VAWTs operate under low wind speed conditions and are favorable for small-scale power generation [6]. Therefore, VAWTs have recently received a growing interest in energy harvesting in urban environments [7]. VAWTs advantages include simple construction, low manufacturing, installation and maintenance costs, omnidirectional capability [8],

* Corresponding author.

E-mail addresses: mahmoud.ahmed@ejust.edu.eg, aminism@aun.edu.eg (M. Ahmed).

Nomenclature	
A	Rotor cross-sectional area [m^2]
AR	Aspect Ratio (H/D) [-]
C_H	Dynamic thrust coefficient [-]
C_{HS}	Static thrust coefficient [-]
C_P	Power coefficient [-]
$C_{P_{max}}$	Maximum power coefficient [-]
C_T	Torque coefficient [-]
C_{TS}	Static torque coefficient [-]
D	Rotor rotating diameter [m]
D_O	Diameter of endplates [m]
d	Blade chord length [m]
e	Overlap distance [m]
F_H	Dynamic thrust force on the rotor (N)
F_{HS}	Static thrust force on the rotor (N)
H	Rotor height [m]
HAWTs	Horizontal Axis Wind Turbines [-]
k	Turbulent kinetic energy [m^2/s^2]
N	Rotational speed [rpm]
P_{rotor}	Mechanical power of rotor [W]
P_{wind}	Available wind power [W]
R^2	Correlation coefficient [-]
RNG	Renormalization Group [-]
SIMPLE	Semi-Implicit Method for Pressure-Linked Equations [-]
SST	Shear Stress Transport [-]
T	Dynamic torque [N. m]
T_S	Static torque [N. m]
u_t	Rotor tip speed [m/s]
V	Wind speed [m/s]
VAWTs	Vertical Axis Wind Turbines [-]
y^+	Dimensionless wall distance [-]
δ	Overlap ratio (e/d) [-]
θ	Rotor angle [$^\circ$]
λ	Tip speed ratio (u_t/v) [-]
ρ	air density [kg/m^3]
φ	Twist angle [$^\circ$]
ω	Specific dissipation rate [1/s]
ω_r	Angular velocity of the rotor [rad/s]

relatively high self-starting capabilities and lower aerodynamic noise [9]. Furthermore, VAWTs are capable of capturing highly unstable and turbulent wind flows which are typical patterns in urban environments [10].

Savonius rotors are included in VAWTs and so generate high starting torque in any wind direction with low cut-in wind speed and operate silently at a very low tip speed [11]. Thus, the Savonius rotor is useful as a low-cost, small-scale decentralized energy generation device [12]. It usually consists of two cylindrical halves facing opposite directions in an S-shape (for a two-bladed rotor) [13]. The basic working principle is based on the difference of the momentum force which transforms into pressure difference between the convex and the concave surfaces of the rotor blades as they rotate around a vertical shaft. However, at small rotor angles (θ), the contribution of the lift force in the net torque generation has been reported by Modi and Fernando [14]. The aspect ratio (AR), overlap ratio (δ), number of blades, end plates, number of stages and blade shape are geometrical parameters that influence the performance of a conventional Savonius rotor. It has been reported by several investigations that the performance has increased significantly through parametric optimization.

Sheldahl et al. [15] investigated experimentally the performance of the Savonius rotor with two aspect ratios of 1.0 and 1.5 at a constant overlap ratio of 0.15. Their results showed that the trends of power and torque coefficients for an aspect ratio of 1.0 were similar to the aspect ratio of 1.5, with a slight increase for aspect ratio 1.5. A three-dimensional flow analysis was conducted by Ferrari et al. [16] on the Savonius rotor with four aspect ratios of 0.55, 0.78, 1.1, and 1.66 at an overlap ratio of 0.2. It was observed that the power coefficient significantly increased by raising the aspect ratio from 0.55 to 1.1 and slightly increased in the range of 1.1–1.66. Bhayo and Al-Kayiem [17] found a significant improvement in the modified conventional Savonius rotor performance with increasing the aspect ratio from 0.77 to 2.0.

It has been reported that conventional Savonius rotors with overlapping blades have a better performance and self-starting ability compared to those without overlap [15]. The overlap between two semi-circular blades causes air from the concave side of the advancing blade to pass through the overlap region. Due to the overlap region, the pressure on the concave side of the returning blade increases, and in return reduces the pressure difference between the concave and convex side. This results in decreasing the net torque generated by the returning blade and increasing the net torque for the whole blades [18].

Therefore, several studies were carried out on conventional Savonius rotors to determine the optimum overlap ratio that attains a

maximum power coefficient. Kianifar et al. [19] studied the effect of overlap ratios on the performance of a conventional rotor with an aspect ratio of 1.875. Their results showed a significant increase in the power coefficient with increasing the overlap ratio from 0 to 0.2 as a result of decreasing resisting forces. On the other hand, increasing the overlap ratio from 0.2 to 0.45 reduces the power coefficient with the optimum value at 0.2. Fujisawa [20] experimentally studied the influence of the overlap ratio on aerodynamic performance and flow fields by measuring the pressure distribution on blades and visualizing the flow fields in and around the rotors for both static and dynamic cases. Experiments were performed using a two-blade Savonius rotor with various overlap ratios ranging from 0 to 0.5. Flow observations near the overlap indicated that the flow separation increased with the overlap ratio that reduced the aerodynamic performance at large overlap ratios. The maximum torque and power were observed at an overlap ratio of 0.15. Akwa et al. [21] numerically studied the influence of various overlap ratios ranging from 0 to 0.6 on the performance of the conventional Savonius rotor. Similar results showed the best performance at an overlap ratio of 0.15. Jian et al. [22] studied the influence of overlap ratios of 0, 0.167, and 0.333 on the performance of a conventional rotor with an aspect ratio of 1.088. Their results showed that an overlap ratio of 0.167 attained the best power coefficient.

With an increasing number of blades, fluctuations of both dynamic and static torque coefficients of a conventional Savonius rotor can be reduced, and the power coefficient was found to be decreased [23]. Sheldahl et al. [15] tested two- and three-bladed Savonius rotors with aspect and overlap ratios of 1.0 and 0.15, respectively. It was found that a two-bladed Savonius rotor had a higher power coefficient than the three-bladed rotor. Emmanuel et al. [24] performed a two-dimensional analysis to investigate the performance of a conventional Savonius rotor using multi-bladed rotor and external shield to prevent the wind from impinging on convex surfaces of the blades. The studied rotors have an aspect ratio of 2.0 and 2 and 6 number of blades. The results showed that the six-bladed Savonius wind rotor has a better self-starting ability than the conventional two-bladed one. In order to determine an optimum number of blades, Mahmoud et al. [25] experimentally studied the performance of a Savonius rotor with a single- and double-stage at a zero-overlap ratio. It was found that a two-bladed rotor attained better performance than three- and four-bladed rotors for single- and double- stage.

Using endplates at the conventional Savonius rotor tips is the simplest method to improve performance. Savonius rotors with high aspect ratios display better performance due to low losses from rotor tips

however, most existing rotors were installed with low aspect ratio to avoid structure failure [26]. Hence, it is recommended to use endplates that have a similar influence on higher aspect ratios to improve the performance of low aspect ratio rotors [27]. Wind velocity was the most important parameter that defined the characteristics of fluid flow around a Savonius wind turbine. Kamoji et al. [28] studied the effect of wind velocity using Reynolds number ranging from 80,000 to 150,000 on the performance of a Savonius rotor with a modified profile. They found that increasing Reynolds number from 80,000 to 150,000 resulted in boosting the power coefficient by 19%, and the static torque coefficient was almost independent of the Reynolds number. Hayashi et al. [29] and Kamoji et al. [30] also reported that the power coefficient increased with an increase in the Reynolds number for a conventional one-, two- and three-stage Savonius rotor. Alom and Saha [31] studied the influence of three different Reynolds number values including 0.72×10^5 , 0.89×10^5 and 1.01×10^5 . This corresponded to wind velocities of 5 m/s, 6.2 m/s and 7 m/s on the performance of the Savonius rotor with various blade profiles. It is found that the power coefficient increased with the increase of Reynolds number.

From the above-mentioned literature, it was found that the conventional Savonius rotor displays a better performance with an aspect ratio in the range of 1.0–2.0. Moreover, the value of the overlap ratio achieving the best performance ranged between 0.15 and 0.2. The power coefficient of a two-bladed rotor is higher than that of a three-bladed rotor; as a three-bladed rotor requires a higher starting static torque. The use of endplates exhibited a similar influence on higher aspect ratios, as they improve the performance of Savonius rotors with low aspect ratios. The power coefficient is enhanced by increasing the Reynolds number however, the static torque coefficient is almost independent of Reynolds numbers.

The disadvantages of a conventional single-stage Savonius rotor included a large oscillation of torque coefficients with negative values at some rotor angles [26]. Therefore, the stacking of a single-stage rotor in a series pattern (multi-stage) with a phase shift is expected to smooth

the variations in the torque coefficient and produce positive values at all rotational angles. In two stages, one single-stage rotor is placed over another single stage with a 90° phase shift. In three stages, the three single-stage rotors are placed one above the other with a phase shift of 60° relative to one another [32]. Kamoji et al. [30] studied the performance of a single-, two-, and three-stage Savonius rotor in order to obtain the optimum number of stages. Their results showed a higher static torque coefficient with a low variation for multi-stage rotors. However, the use of a multi-stage rotor significantly reduced the power coefficient compared to a single-stage rotor. Kumar et al. [33] carried out an experimental and numerical investigation on one, two, and three stages of the Savonius rotor to improve the performance of the rotor and reduce the thrust load. The results indicated that the three stages of the Savonius rotor attains better self-starting ability and a significant reduction of 58% on the thrust load compared to the single-stage rotor. However, the three stages showed a lower maximum power coefficient of 0.14.

In summary, using twisted blades could be a viable approach to enhance the Savonius rotor performance in terms of achieving a higher power coefficient, and starting ability along with smooth device operation compared to the conventional untwisted rotors. However, a closer look at the design parameters showed a lack of clear analysis related to the effect of such parameters on the performance of the twisted-bladed Savonius rotor. Therefore, the originality of the current work is based on two main concepts. First, a comprehensive three-dimensional, incompressible unsteady Reynolds-averaged Navier-Stokes model in conjunction with k- ω shear-stress transport turbulence model is developed. This model will predict the effect of various parameters including twist angle (φ), overlap ratio (δ), endplate size ratio (D_0/D), and wind velocity (V) on the performance of the Savonius rotor wind turbine. Second, novel assessment methods based on flow field characteristics such as streamlines and pressure fields around the Savonius wind turbine are carried out. This is the first contribution to understand how geometrical variables influence the aerodynamic performance of

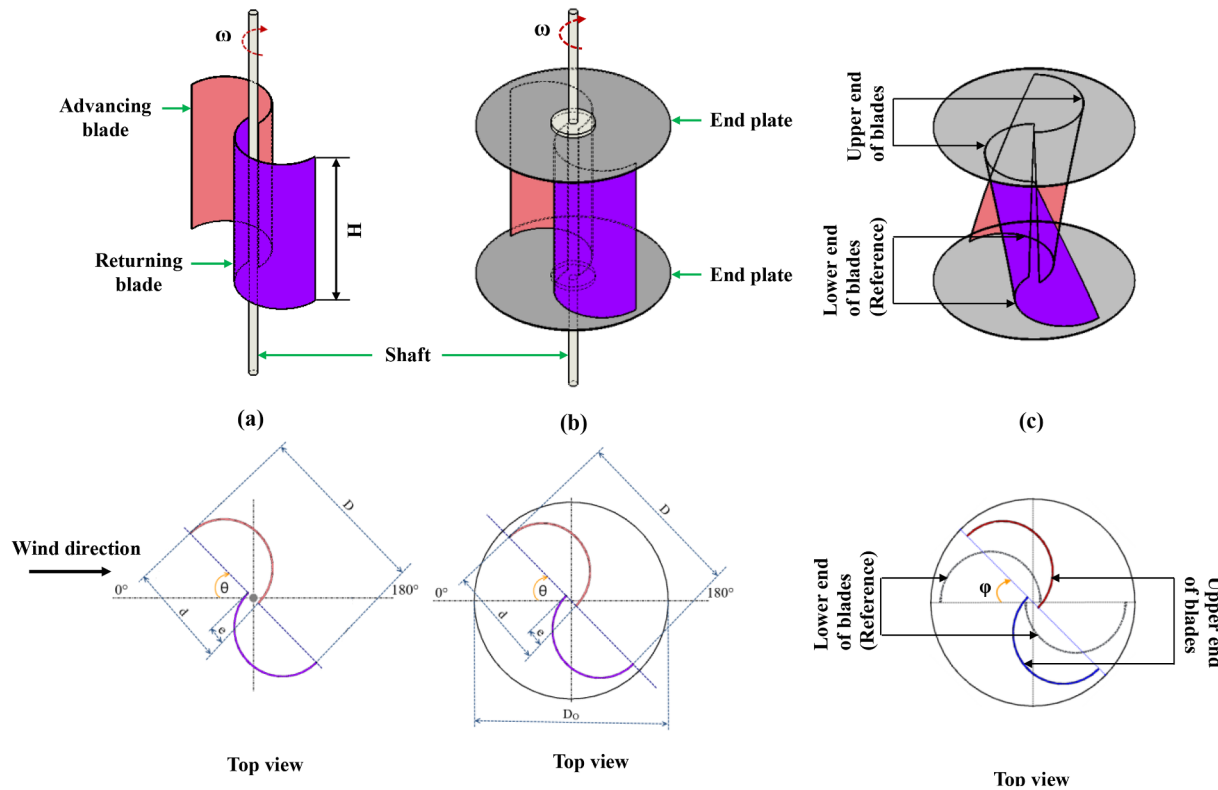


Fig. 1. A neat schematic description and main geometric parameters of (a) a typical Savonius rotor without endplates, (b) a typical Savonius rotor with endplates, and (c) the proposed Savonius rotor with twist angle (φ).

the twisted Savonius rotor. Moreover, the variation of torque, power, thrust, and static torque coefficients are estimated. Consequently, the best design variables are recommended for practical applications.

2. Physical model

A neat sketch of a typical Savonius wind turbine and the proposed twisted Savonius wind turbine is shown in Fig. 1. The main components include upper and lower circular endplates and two blades. The whole components are integrated with end rotating shafts connected directly to endplates as presented in Fig. 1-b. However, in the case of no endplates, the two blades are combined with a rotating shaft as shown in Fig. 1-a. The main dimensions include the rotor height (H), the rotor diameter (D), the blade chord (d), the endplates diameter (Do), and the overlap distance (e).

In the current study, the influence of varying several geometrical parameters such as twist angle (φ), overlapping ratio (δ), and the circular end plate size ratio (Do/D) along with wind velocity (V) on the

performance of the proposed twisted Savonius wind turbine is investigated. In addition, the rotor diameter is kept constant at 400 mm, with a thickness of 2 mm, and aspect ratio, AR = H/D at unity. Fig. 1-c presents the twist angle (φ) which is defined as the angle between the lower (reference) and upper ends of the twisted rotor. The studied twist angles are 0°, 45°, 90°, 135°, and 180°. Additional investigated geometrical parameters include the overlapping ratio ($\delta = e/d$) defined as the ratio of overlap distance between the blades (e) and blade chord length (d). Fig. 2-a show how the overlapping ratio varies from zero to 0.3. The last studied geometrical parameter is the circular end plate size ratio (Do/D). In the current work, this ratio is varied from zero to 1.2 as depicted in Fig. 2-b. Finally, the twisted Savonius wind turbine is exposed to a free stream wind velocity varied from 4 to 18 m/s.

3. Theoretical analysis

In the present work, a comprehensive 3-D unsteady incompressible turbulent flow around the twisted Savonius wind turbine is developed.

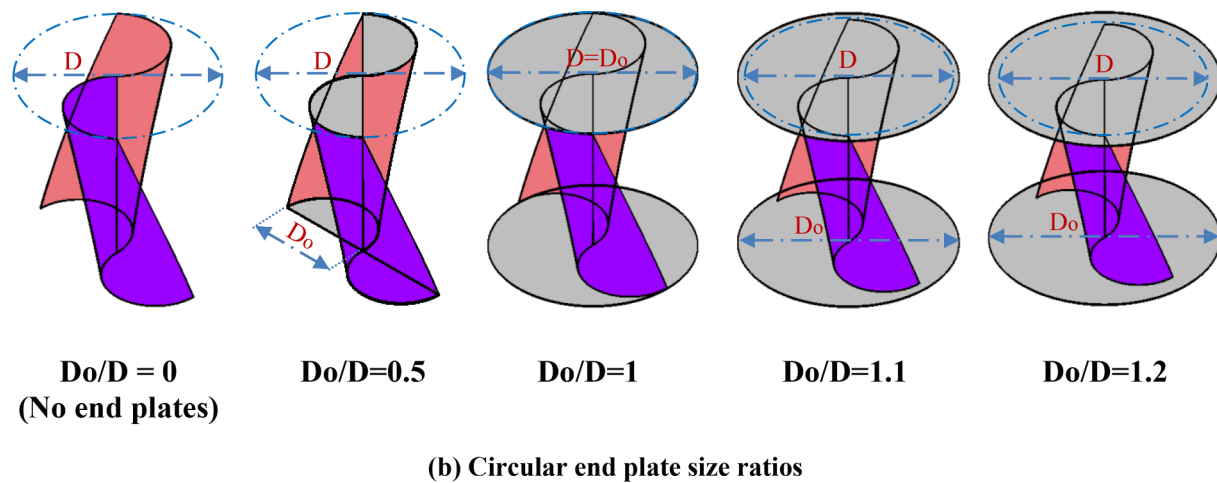
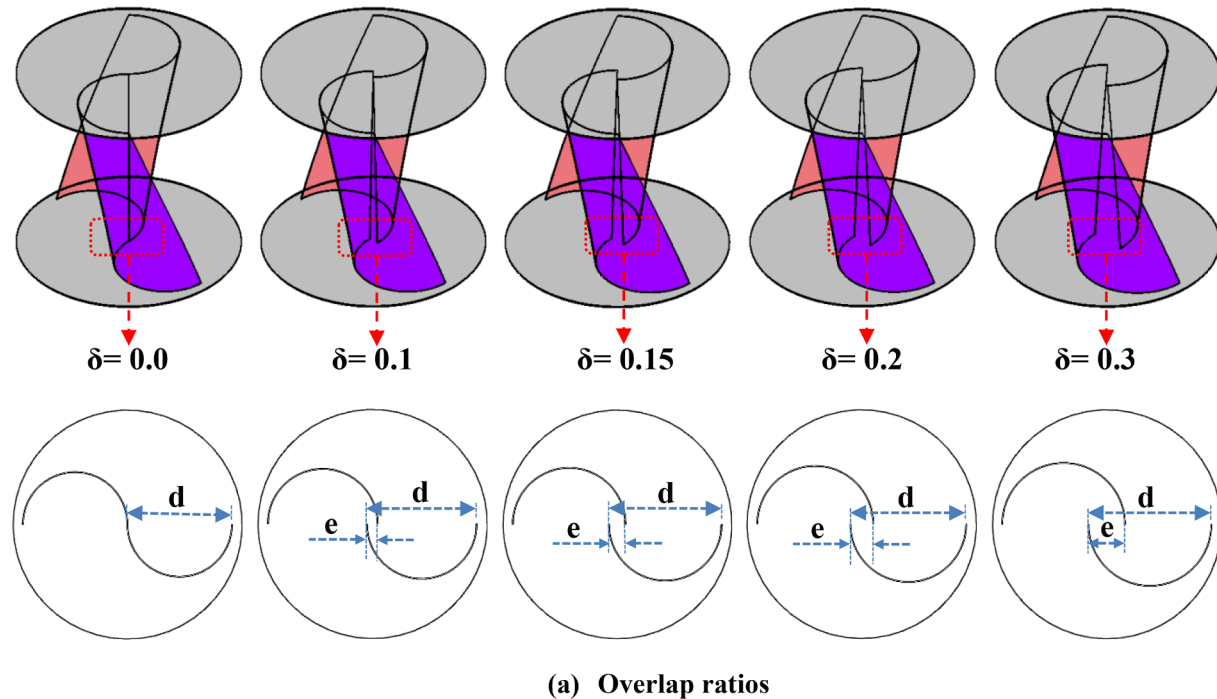


Fig. 2. A neat schematic sketch of studied geometrical parameters for the proposed twisted Savonius rotor: (a) Overlap ratios (δ) (b) Circular end plate size ratios (Do/D).

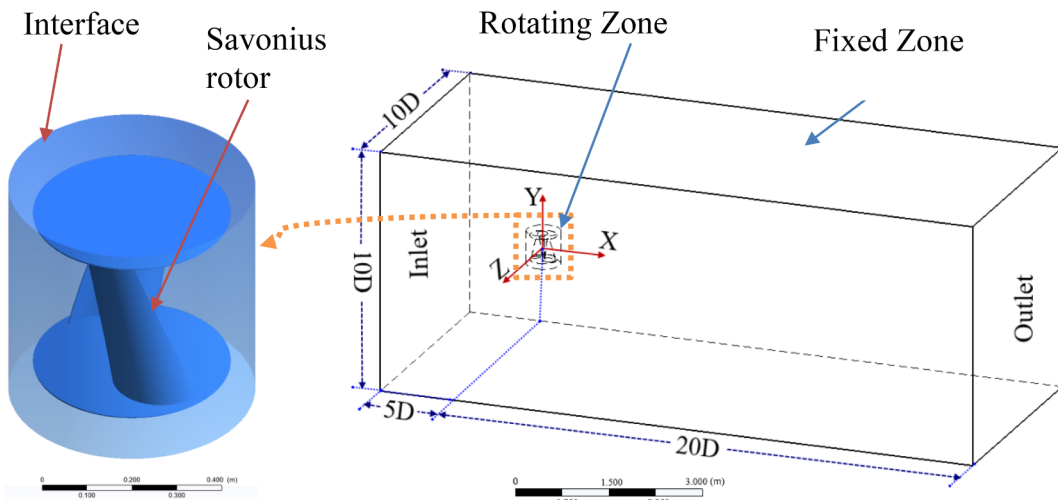


Fig. 3. Schematic representation of the computational domain.

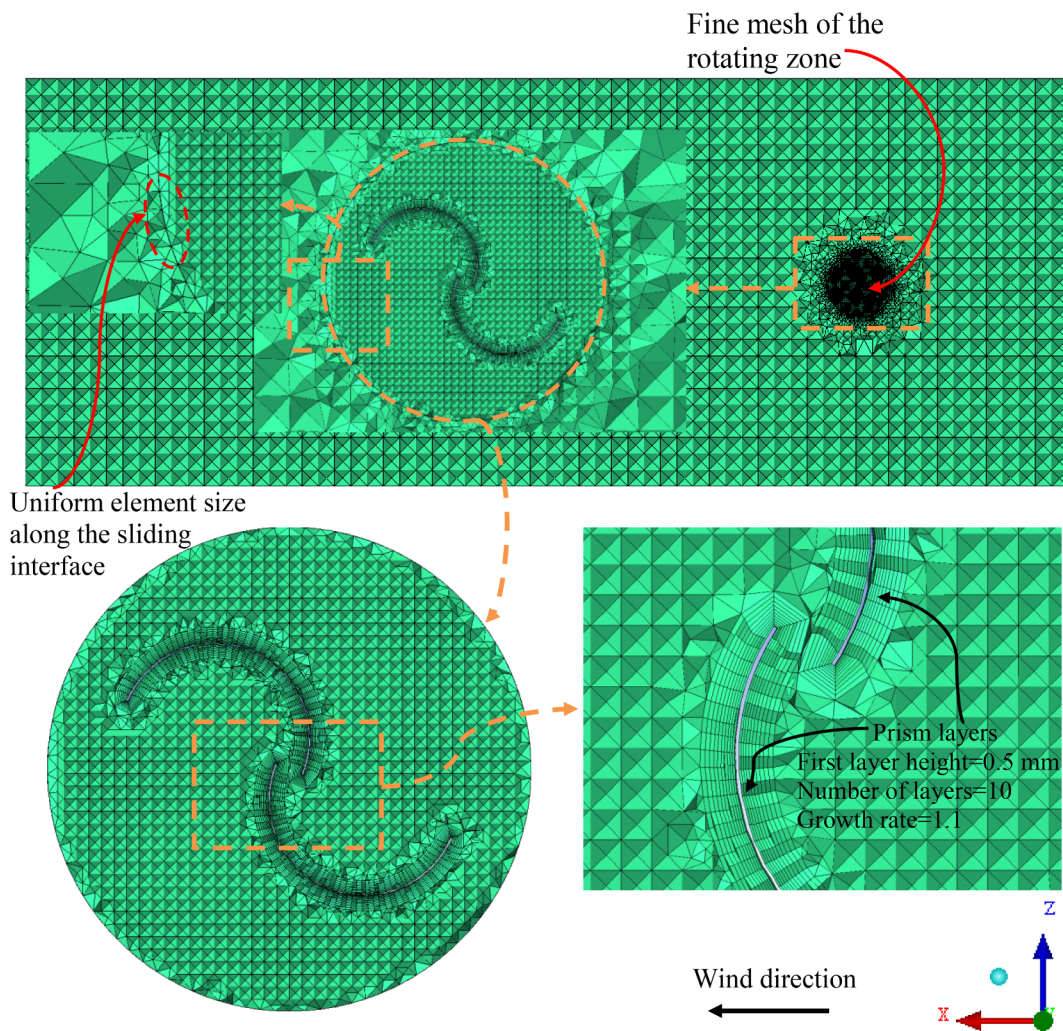


Fig. 4. Grid generation for the computational domain and the boundary layers.

The model includes Reynolds-Averaged Navier-Stokes equations [34] in conjunction with the SST k- ω turbulence model [35]. The governing equations for unsteady Newtonian incompressible turbulent flow can be written in a tensor form as follows:

$$\frac{\partial \bar{u}_i}{\partial x_i} = 0 \quad (1)$$

$$\frac{\partial \bar{u}_i}{\partial t} + \bar{u}_j \frac{\partial \bar{u}_i}{\partial x_j} = -\frac{1}{\rho} \frac{\partial \bar{P}}{\partial x_i} + \frac{\mu}{\rho} \frac{\partial^2 \bar{u}_i}{\partial x_j^2} - \frac{\partial}{\partial x_j} (\bar{u}'_i \bar{u}'_j) \quad (2)$$

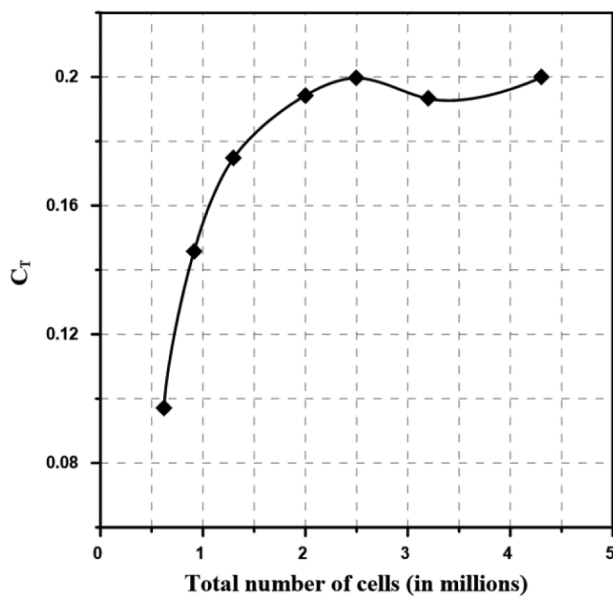


Fig. 5. Averaged torque coefficient over a complete revolution versus the number of cells at $\lambda = 0.8$.

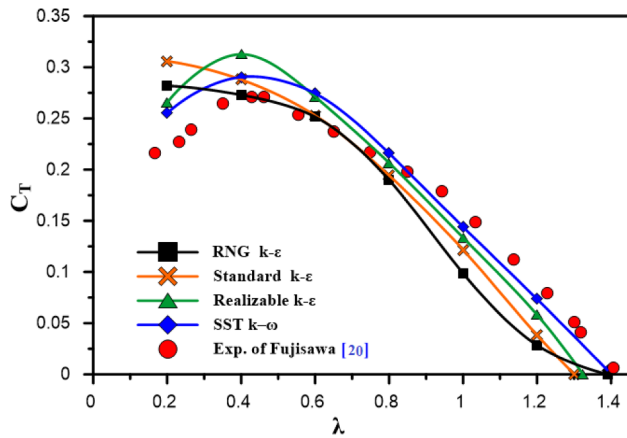


Fig. 6. Comparison between predicted results using different turbulence models and experimental results of Fujisawa [20].

Table 1
The correlation coefficient (R^2) for the studied turbulence models.

Turbulence model	R^2
Standard $k-\epsilon$	0.774
Realizable $k-\epsilon$	0.885
RNG $k-\epsilon$	0.782
SST $k-\omega$	0.943

$$\frac{\partial}{\partial t}(\rho\kappa) + \frac{\partial}{\partial x_j}(\rho\kappa u_j) = \frac{\partial}{\partial x_j} \left[\left(\mu + \frac{\mu_t}{\sigma_\kappa} \right) \frac{\partial \kappa}{\partial x_j} \right] + G_\kappa - Y_\kappa \quad (3)$$

$$\frac{\partial}{\partial t}(\rho\omega) + \frac{\partial}{\partial x_j}(\rho\omega u_j) = \frac{\partial}{\partial x_j} \left[\left(\mu + \frac{\mu_t}{\sigma_\omega} \right) \frac{\partial \omega}{\partial x_j} \right] + G_\omega - Y_\omega \quad (4)$$

where: \bar{u}_i is the mean flow velocity and u'_i is the fluctuation velocity. x_i is the coordinate system; t is the time; \bar{P} is the mean pressure while μ and ρ represent the dynamic viscosity and density of air, respectively. G_κ represents the generation of turbulence kinetic energy due to the mean velocity gradient. Y_κ represents the dissipation of turbulence kinetic energy; G_ω represents the generation of ω , Y_ω represents the

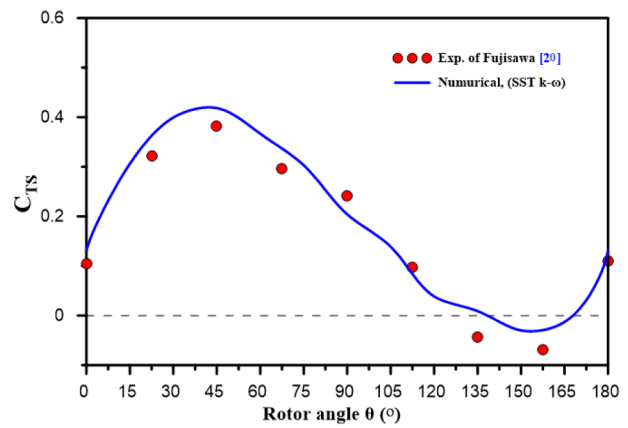


Fig. 7. Comparison between the predicted static torque coefficient versus rotor angle and experimental results of Fujisawa [20].

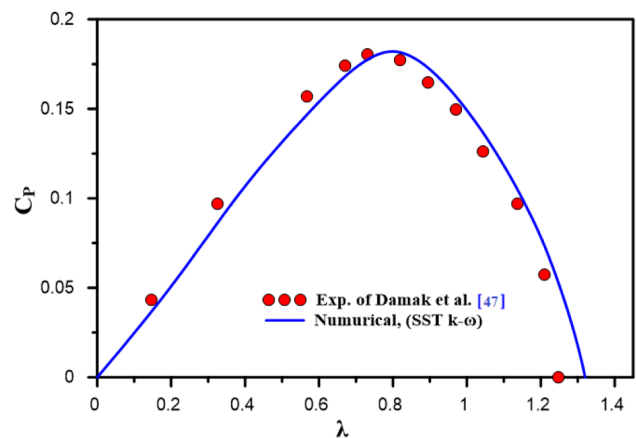


Fig. 8. Comparison between power coefficient versus tip speed ratio and experimental results of Damak et al. [47].

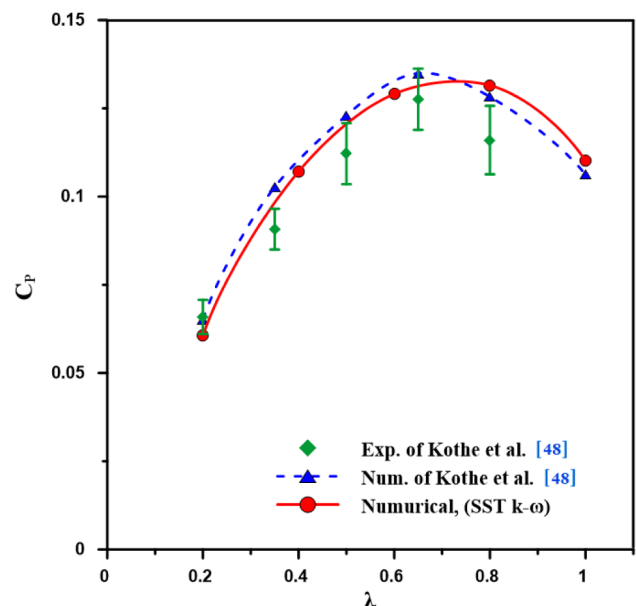


Fig. 9. Comparison between the predicted power coefficient versus tip speed ratio and experimental and numerical results of Kothe et al. [48].

dissipation of ω ; σ_κ , σ_ω are turbulent Prandtl numbers for κ , ω , and μ_t represents the turbulent (or eddy) viscosity. Plourde et al. [36] carried out a three-dimensional unsteady simulation along with $k-\omega$ shear-

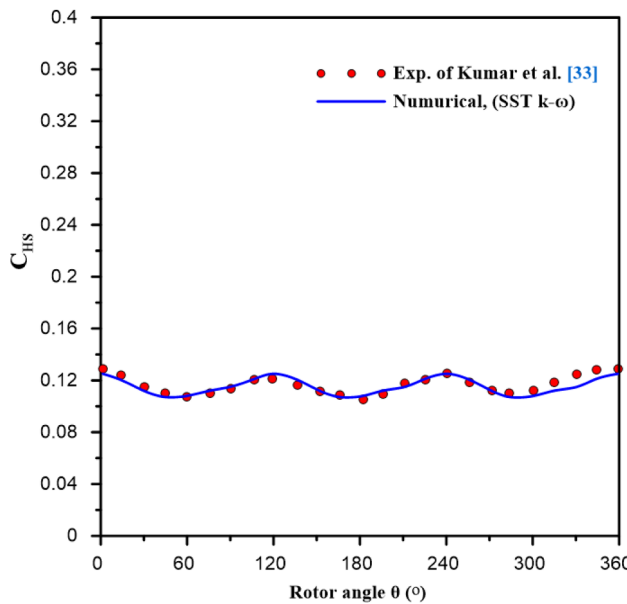


Fig. 10. Comparison between the predicted static thrust coefficient versus rotor angle and the experimental results of Kumar et al. [33].

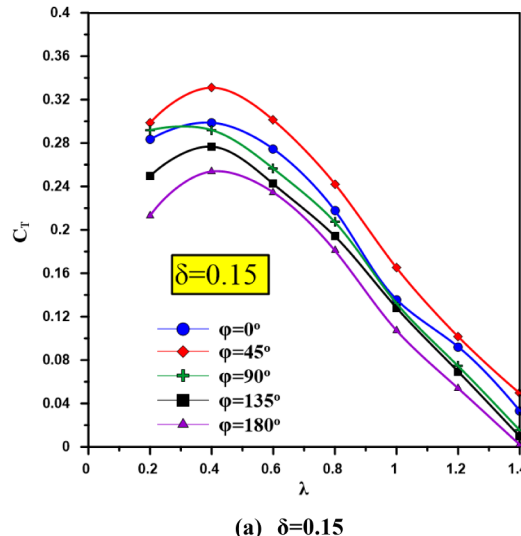
stress transport (SST) turbulence model on Savonius wind turbine and found results in a good agreement with experiments. Fertahi et al. [37] carried out a two-dimensional transient analysis on a hybrid Savonius-Darrieus rotor while Wong et al. [38] carried out a three-dimensional unsteady analysis on a vertical axis wind turbine with flat plate deflector using SST k- ω turbulence model. Both studies reported that the predicted results obtained using SST k- ω turbulence model were in a good agreement with experiments. The same finding was reported by Tian et al. [39] and Ostos et al. [40].

3.1. Performance parameters

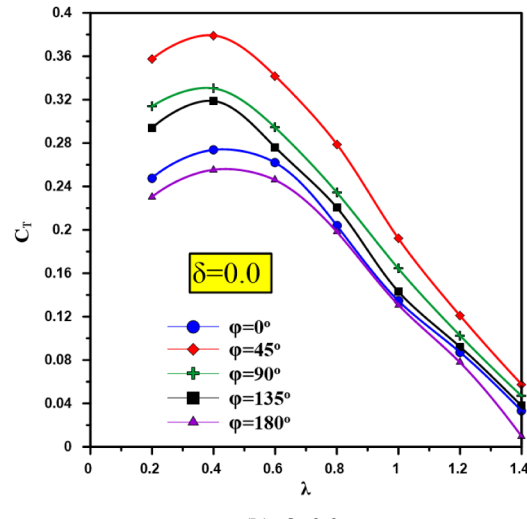
The power coefficient (C_p) of the Savonius rotor is defined as the ratio of the actual mechanical power (P_{rotor}) generated by the rotor to the available wind power (P_{wind}) [26] and can be expressed by:

$$C_p = \frac{P_{rotor}}{P_{wind}} = \frac{T \times \omega_r}{0.5\rho AV^3} = \frac{2\pi NT}{60 \times 0.5\rho AV^3} \quad (5)$$

The net rotor torque at a particular rotor angle is given by the



(a) $\delta = 0.15$



(b) $\delta = 0.0$

Fig. 11. The variation of the average torque coefficient with tip speed ratios for various twist angles (ϕ) at (a) $\delta = 0.15$, (b) $\delta = 0.0$.

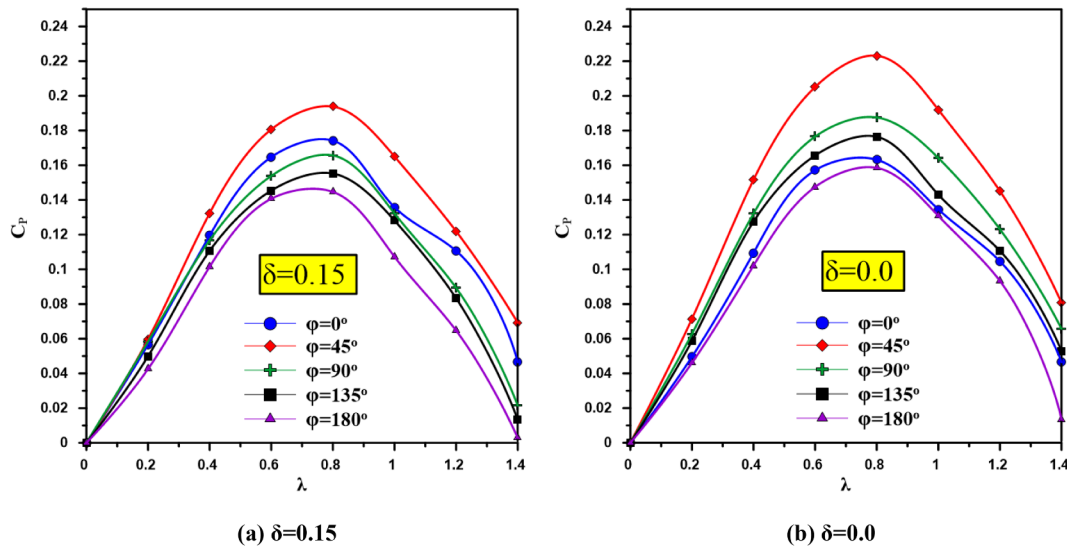


Fig. 12. The variation of the average power coefficient with tip speed ratios for various twist angles (φ) at (a) $\delta = 0.15$, (b) $\delta = 0.0$.

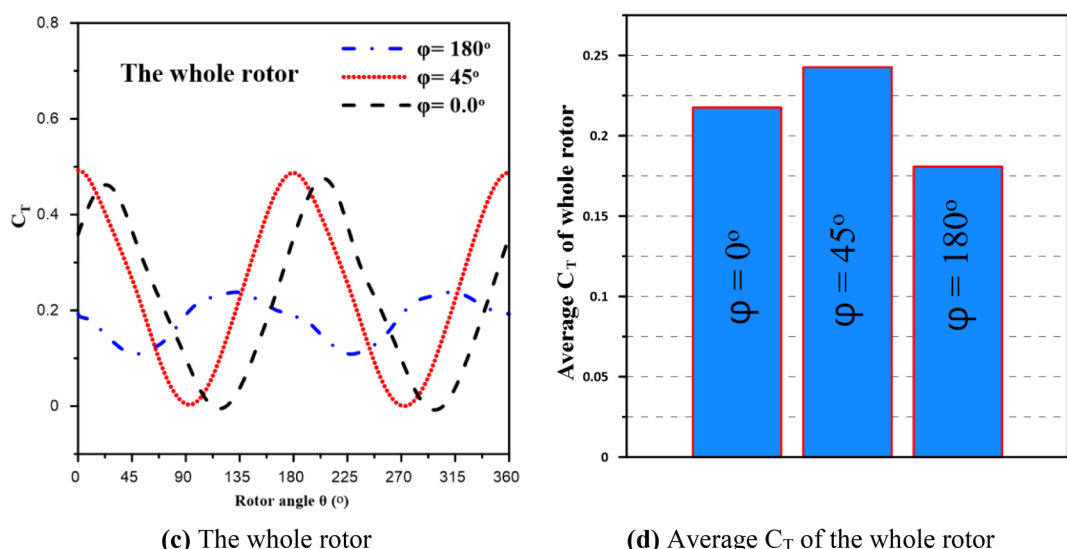
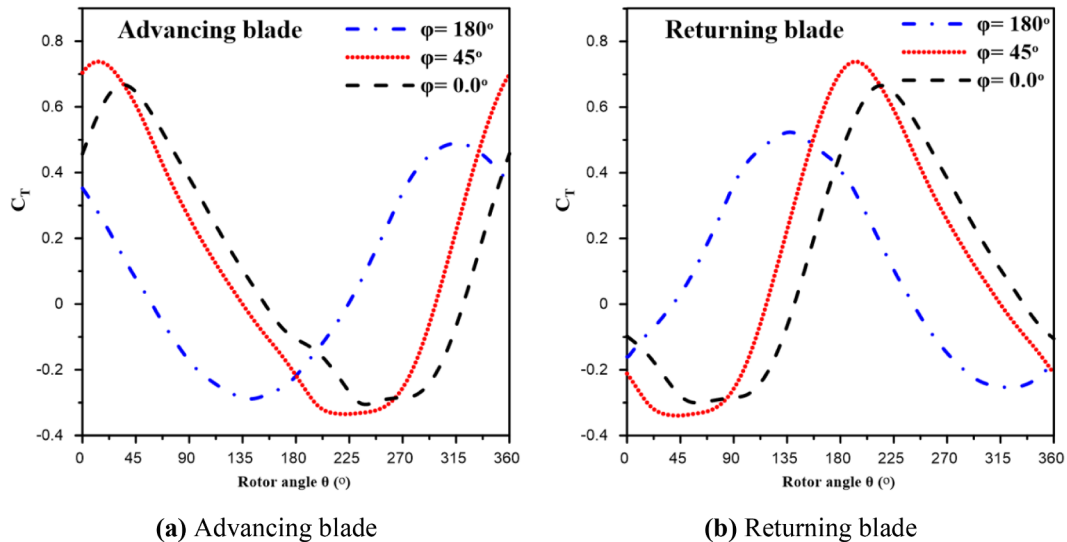


Fig. 13. Instantaneous torque coefficient versus rotor angle over complete revolution for (a) Advancing blade (b) Returning blade (c) The whole rotor, and (d) Average torque coefficient of the whole rotor.

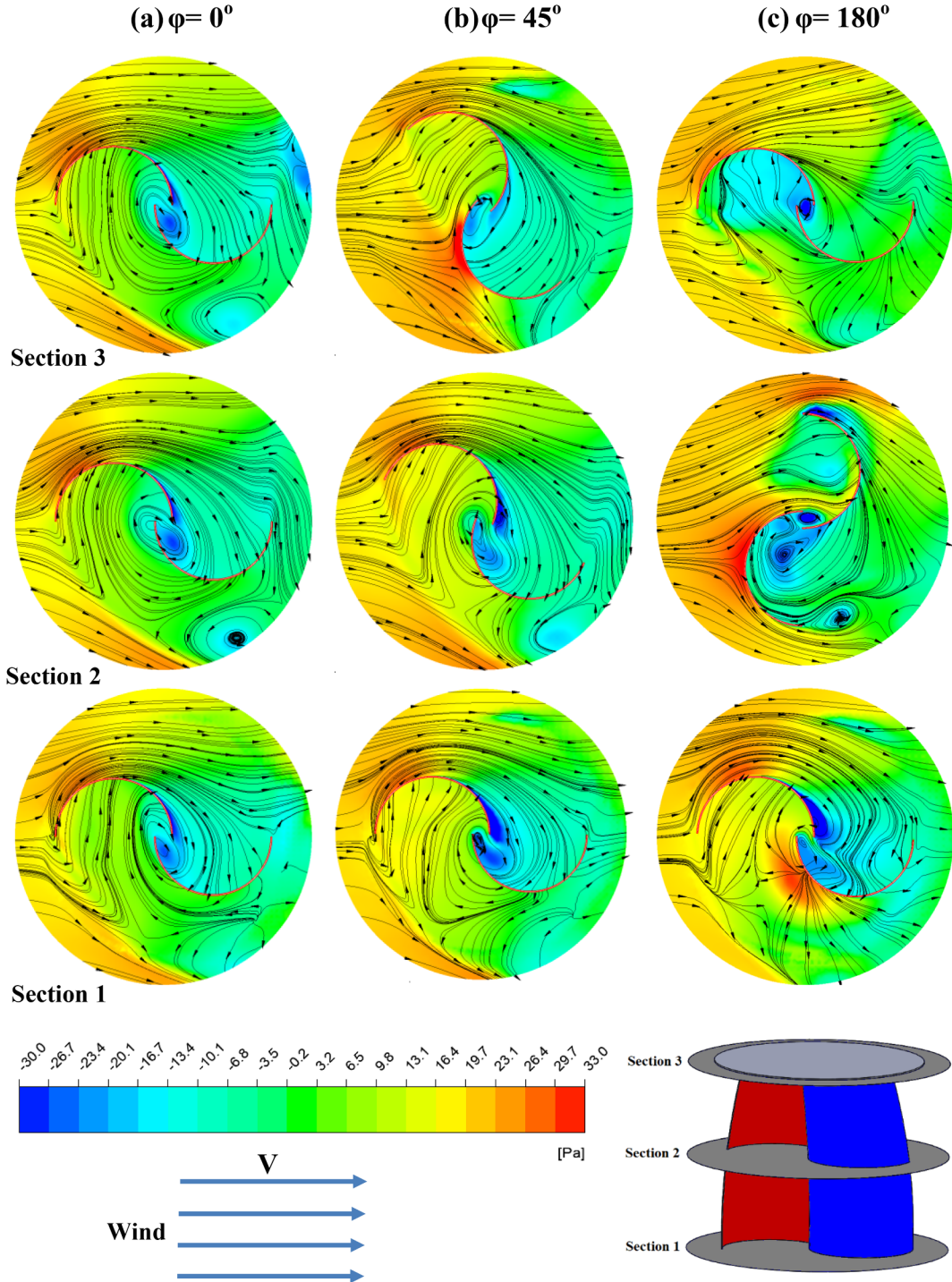


Fig. 14. Sectional total pressure distribution around the blades at rotor angle $\theta = 0^\circ$ for (a) $\varphi = 0^\circ$, (b) $\varphi = 45^\circ$, (c) $\varphi = 180^\circ$.

field and the rotating zone was allowed to rotate with different rotational speeds while the second zone was kept fixed.

4. Numerical solution

In the present study, the governing equations of three-dimensional Newtonian incompressible turbulent flow along with boundary and initial conditions are developed. The model equations are numerically simulated using ANSYS FLUENT 17.2. The spatial discretization of the conservative equations is treated with 2nd order upwind scheme and the temporal terms of the conservative equations are discretized using

2nd order fully implicit temporal scheme. Moreover, The Semi-Implicit Method for Pressure-Linked Equations (SIMPLE) algorithm is used for the pressure–velocity coupling. To precisely model the turbulent flow, a robust turbulence model needed to be considered. The time step size is varied with the number of revolutions, to be equal to the time of one degree (i.e. 1 time step $\cong 1^\circ$ of rotation) of the complete revolution (360°) as reported in [42]. The maximum iterations per time step were taken to be 70. The simulations were run for 5 complete turbine rotations. The convergence criterion was 10^{-5} for all solved equations except for the continuity equation, where the convergence residuals are set to be 10^{-3} . Therefore, parallel computing is implemented using a

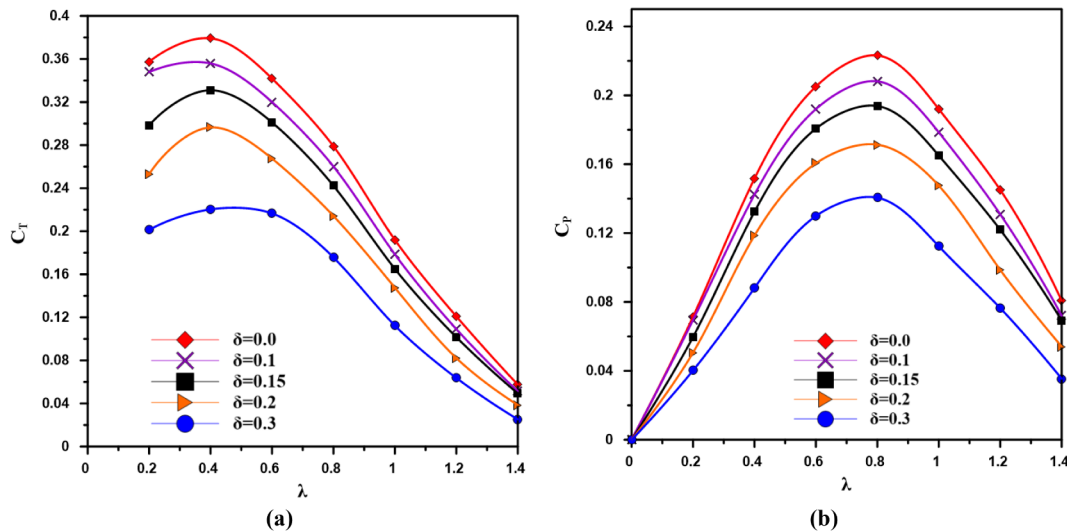


Fig. 15. (a) The variation of the average torque coefficient, (b) The variation of the average power coefficient with tip speed ratios for the studied overlap ratios (δ).

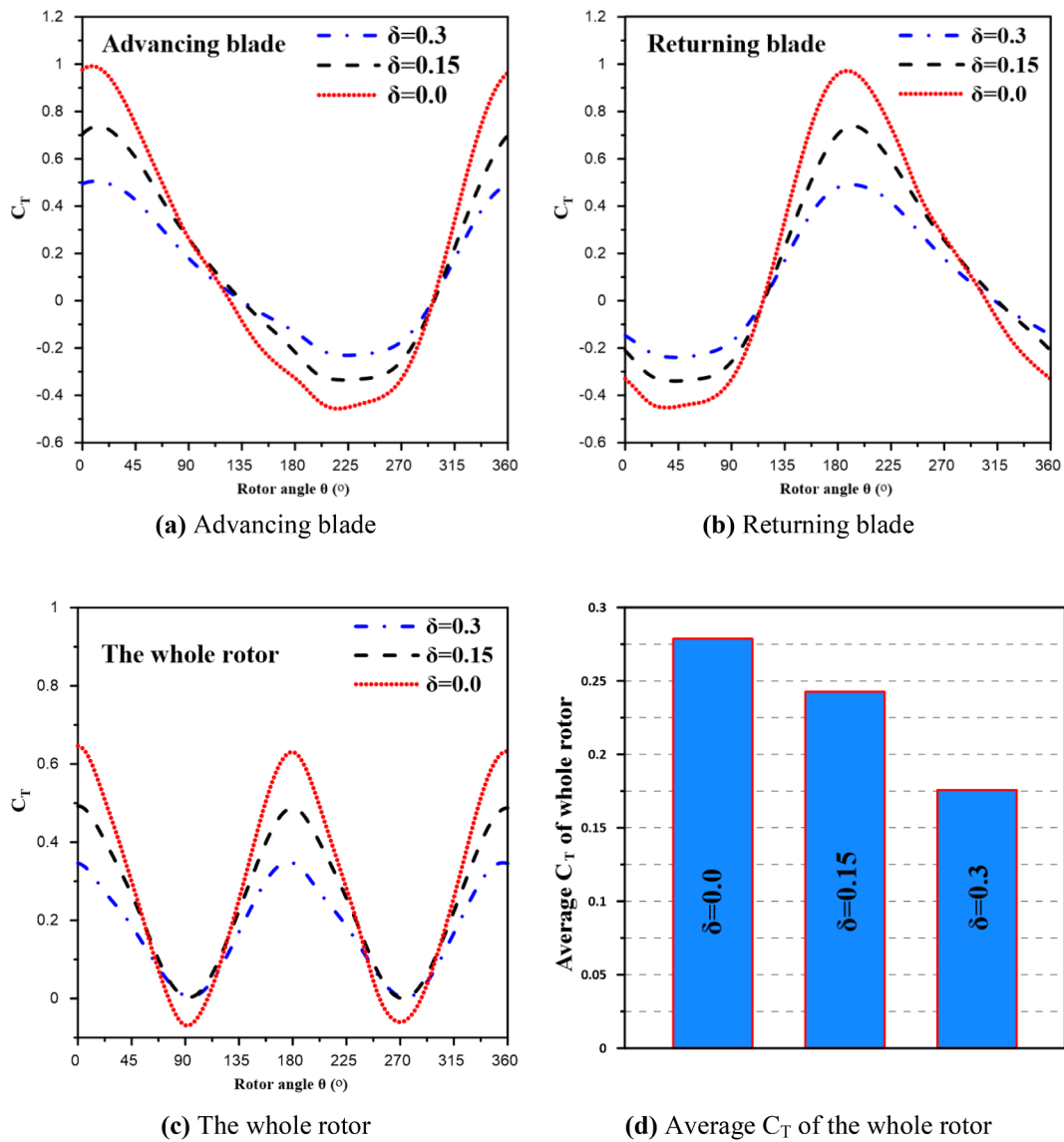


Fig. 16. Instantaneous torque coefficient versus rotor angle over complete revolution for (a) Advancing blade (b) Returning blade (c) The whole rotor, and (d) Average C_T of the whole rotor.

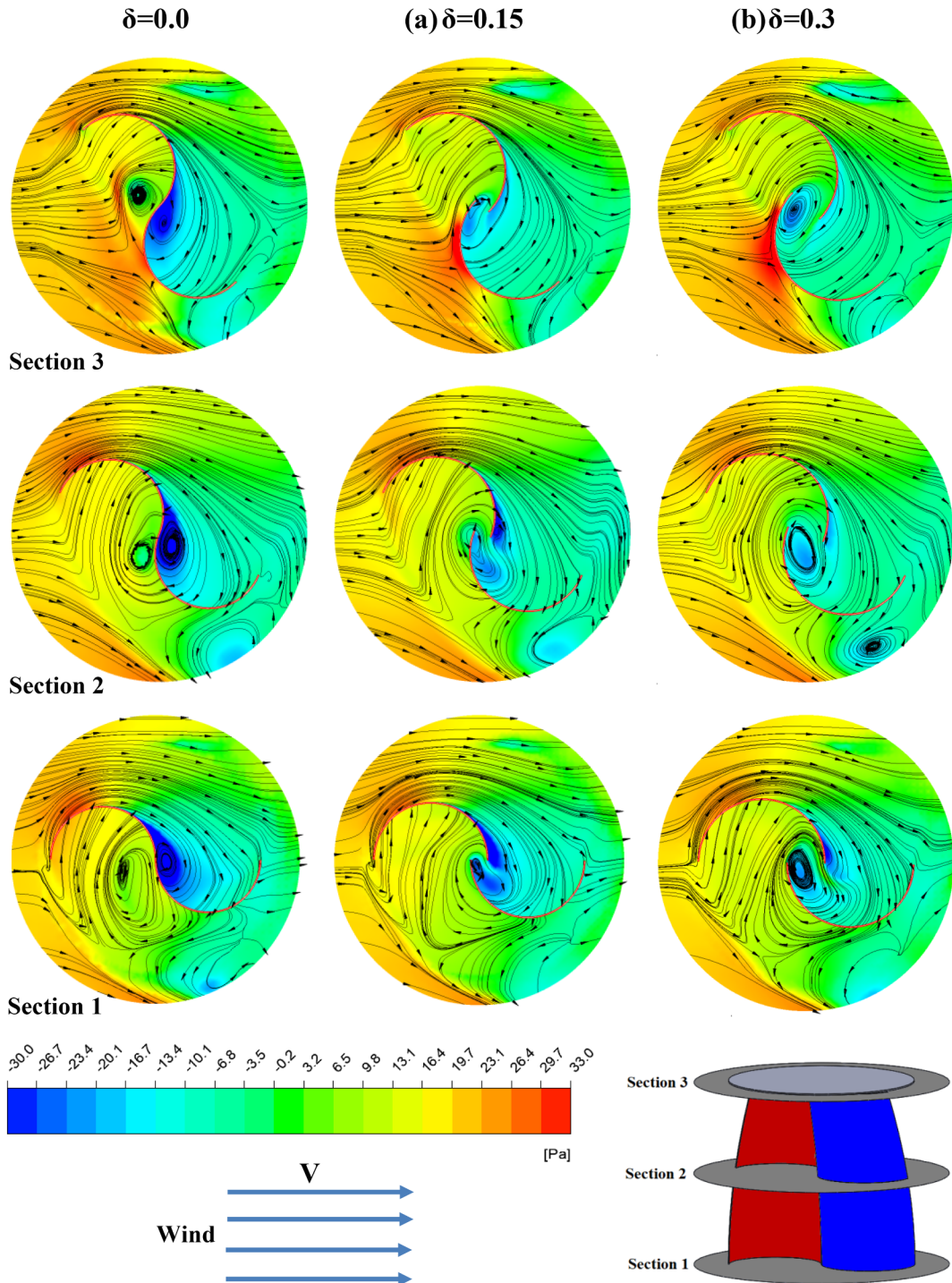


Fig. 17. Sectional total pressure distribution around the blades at rotor angle $\theta = 0^\circ$ for (a) $\delta = 0.0$, (b) $\delta = 0.15$, (c) $\delta = 0.3$.

Dell Precision T7500 workstation with an Intel Xeon® processor of 2.3 GHz, 36-core, and 128-GB installed memory.

4.1. Grid independence study

In the current study, the sliding mesh model [43] was selected to represent the rotation of the Savonius rotor. An unstructured grid with tetrahedral elements is considered to generate mesh for the complete flow domain as shown in Fig. 4. Fine mesh has been created in the rotating region and compared to the stationary zone. The element size was uniform along with the sliding mesh interface. A grid independence

study was performed utilizing the unstructured mesh of suitable grid sizes. Thus, seven different grid numbers of 0.62, 0.912, 1.3, 2, 2.5, 3.2, and 4.3 million cells are tested as shown in Fig. 5. It is found that there are no remarkable variations in all computed parameters with increasing grid numbers over 2.5 million cells. Hence, the 2.5 million cells are retained for all presented computations. In order to capture the boundary layer gradient, the inflation (prism layer) was applied to the rotor wall. According to theoretical derivations and experimental explorations, classifications of the boundary layers are viscous sub-layer ($y+ \leq 5$), buffer layer ($5 < y+ \leq 30$), log-law region ($30 < y+ \leq 500$), and outer layer [44]. For the mesh near the blade's wall, the

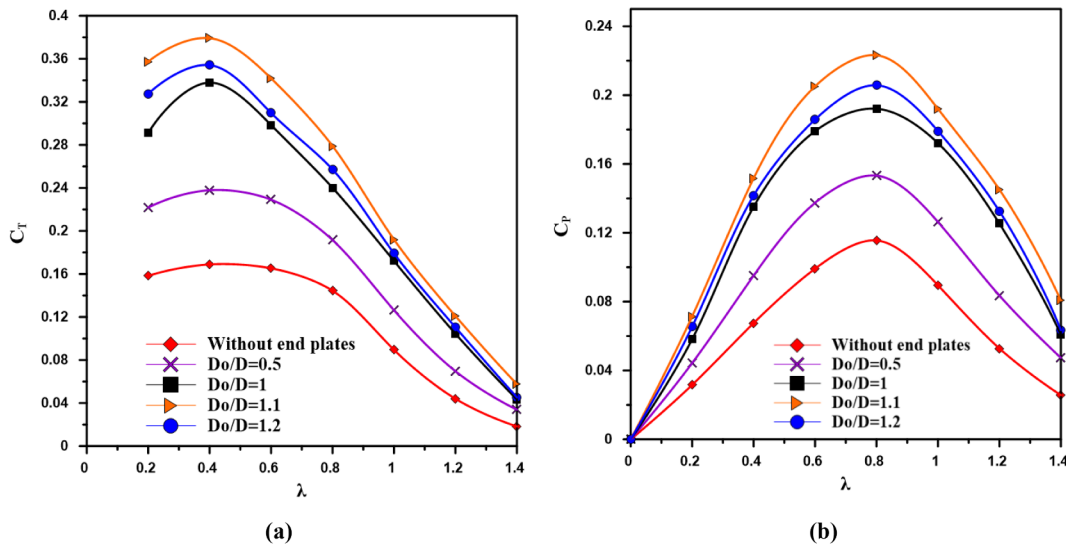


Fig. 18. (a) The variation of the average torque coefficient, (b) The variation of the average power coefficient with tip speed ratios for the studied end plate size ratios (Do/D).

prism layer method was applied to the first layer cell thickness of 0.5 mm, growth rate of 1.1 and a total of 10 layers are selected to obtain maximum y^+ value less than 5 over the rotor blades [45].

4.2. Model validation

To validate the developed model, a comparison between the predicted results and the available numerical and experimental results are carried out. First, Fig. 6 presents the predicted results using four different turbulence models and the experimental results of Fujisawa [20]. The four turbulence models include the standard k- ϵ , the realizable k- ϵ , the RNG k- ϵ , and the SST k- ω . The Savonius rotor tested by Fujisawa [20] has a 30 cm diameter with an overlap ratio (δ) of 0.15 and an aspect ratio (AR) of 1.0. The upstream wind speed was 6 m/s. The predicted results are correlated with the measurements of Fujisawa [20] and the coefficient of correlation (R^2) [46] was used to determine which turbulence model has more accurate results compared with measurements. The values of the correlation coefficient for the studied turbulence models are shown in Table 1. Accordingly, results obtained using the SST k- ω turbulence model attains the highest R^2 of 0.943. Therefore, the SST k- ω turbulence model is more accurate compared to other studied models and will be used in the present simulation.

Second, Fig. 7 presents the predicted static torque coefficient versus the rotor angle using the SST k- ω turbulence model and the corresponding measurements of Fujisawa [20]. A good agreement was found between predicted values and measurements of the static torque coefficient with a maximum deviation of about 4.3%. The deviation is most likely due to the uncertainty of the pressure measurements of Fujisawa [20] which was $\pm 5\%$.

Third, Fig. 8 shows the comparison between the predicted power coefficient and measurements of Damak et al. [47]. They used helical Savonius rotor with a twist angle of 90°, rotor diameter of 230 mm, endplates diameter of 254 mm, and an aspect ratio (AR) of 0.7. The measurements were carried out at Reynolds number $Re = 12.1 \times 10^4$. A good agreement with a maximum deviation of about 2% is found between the present predicted results and those obtained by [47]. This encouraged the authors to extend the simulation using the SST k- ω turbulence model.

Fig. 9 shows the variation of the predicted power coefficient versus tip speed ratio and both experimental and numerical results of Kothe et al. [48] using the helical Savonius rotor with a twist angle of 180°. The helical rotor tested by Kothe et al. [48] was 95 mm rotor diameter

and 104.5 mm endplates diameter, with an aspect ratio (AR) of 4. The measurements were carried out at Reynolds number $Re = 4.63 \times 10^3$. A good agreement with a maximum deviation of about 1% is found between the currently predicted results and the numerical results of Kothe et al. [48]. However, the current simulation slightly over predicted the measured values with a maximum deviation of about 10.5%. This is attributed to the measurement uncertainties of Kothe et al. [48] which vary from 2.34% to 12.5%.

Fig. 10 shows the variation of the measured static thrust coefficient (C_{HS}) by Kumar et al. [33] and the current predicted values versus rotor angle over a complete cycle. A single-stage three-bladed Savonius rotor with 200 mm blade cord length, 450 mm rotor diameter, 480 mm endplates diameter, and 150 mm rotor height were tested. The measurements were carried out at Reynolds number $Re = 2 \times 10^5$. A good agreement between predicted and measured results has been found with a maximum deviation of about 2%.

5. Results and discussion

The Savonius vertical axis wind turbine performance parameters include the power coefficient and self-starting ability. Thus, the effects of geometrical parameters such as a twist angles (φ) ranged from 0° to 180°, an overlap ratios (δ) varied from 0 to 0.3, and circular endplates size ratio (Do/D) ranged from 0 to 1.2 along with a wind velocity (V) in the range of 4 to 18 m/s on the performance parameters are discussed in the following subsections:

5.1. Effect of the twist angle

Variations of the predicted torque coefficient with tip speed ratios for various twist angles (φ) at a wind speed of 6 m/s and an overlap ratio (δ) of 0.15 and 0.0 are presented in Fig. 11-a, and b, respectively. For $\delta = 0.15$, the maximum torque coefficient is observed at $\lambda = 0.4$ for all twist angles except 90° where the maximum torque coefficient occurs at $\lambda = 0.3$. In addition, the maximum torque coefficient is found to be 0.33 at a twist angle of 45° while the minimum value is observed at a twist angle of 180°. As seen in Fig. 11-a, at any value of tip speed ratio (λ), the C_T increases with an increase in twist angle up to an optimum value of $\varphi = 45^\circ$ then gradually decreases till $\varphi = 180^\circ$. The twist angle $\varphi = 45^\circ$ causes the blade to consistently face the oncoming flow. This results in increasing the positive torque generated over a complete cycle. However, with a further increase in twist angle beyond

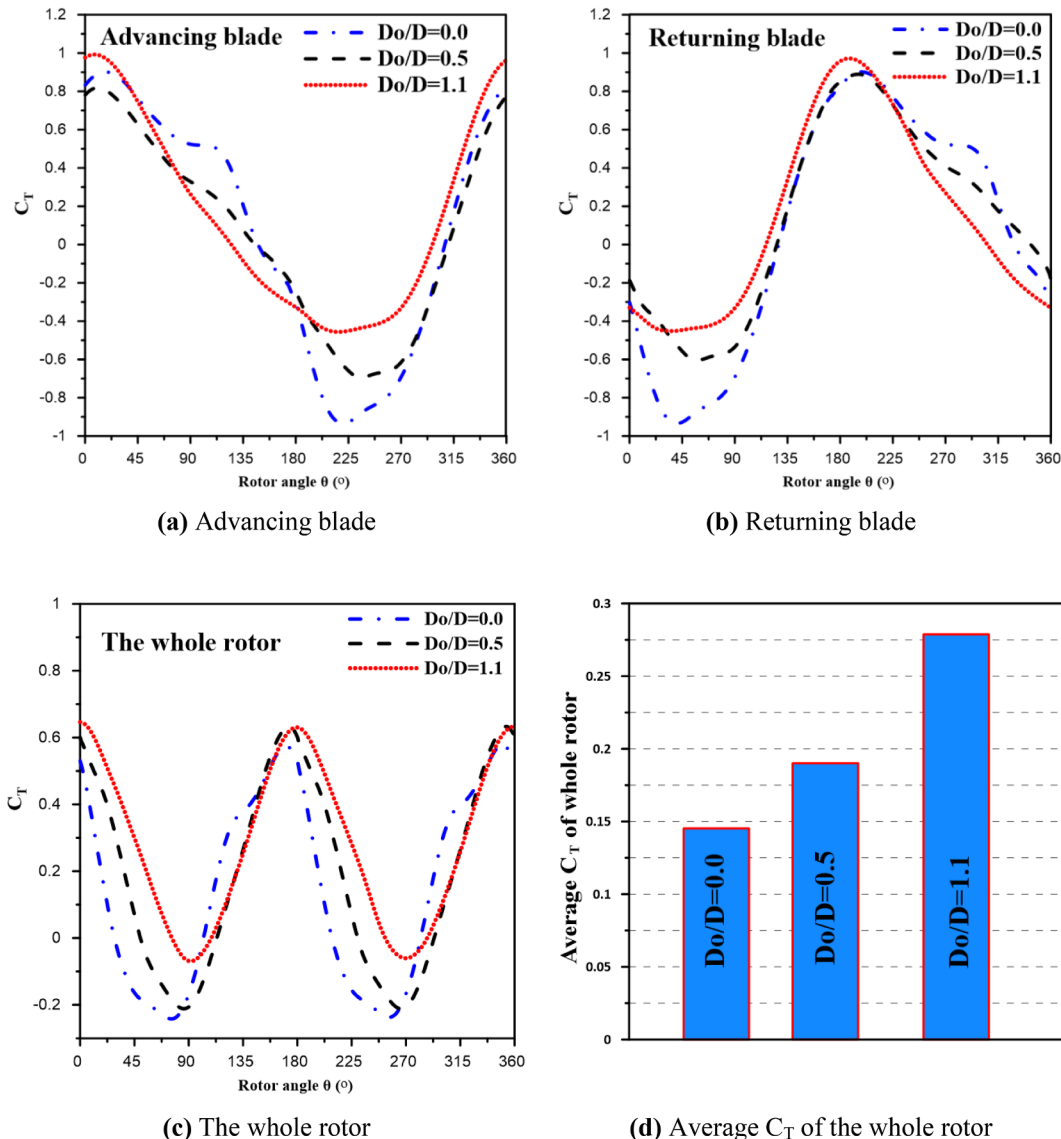


Fig. 19. Instantaneous torque coefficient versus rotor angle over complete revolution for (a) Advancing blade (b) Returning blade (c) The whole rotor, and (d) Average torque coefficient of the whole rotor.

45° (from 90° to 180°), the rotor generates positive torque at all rotor angles and its magnitude gradually decreases with a higher twist angle. This is due to the sharp variation in the blade profile associated with twist angles that increase the distortion of oncoming flow. For $\delta = 0.0$, as shown in Fig. 11-b, a similar trend is shown except $\varphi = 0.0^\circ$ which shows lower C_T compared to $\varphi = 0.0^\circ$ at $\delta = 0.15$. The same finding was previously reported in the literature [20, and 21] where the highest C_T of the conventional untwisted rotor ($\varphi = 0^\circ$) is obtained at $\delta = 0.15$ and it is about 0.38 at a twist angle of 45°.

Fig. 12-a, and b present the variations of predicted power coefficients with a tip speed ratio for various twist angles (φ) at a wind speed (V) of 6 m/s and overlap ratio (δ) of 0.15 and 0.0 respectively. Based on both figures, by increasing the tip speed ratio, the power coefficient increases up to a maximum value at $\lambda = 0.8$. With a further increase of λ beyond 0.8, a significant reduction in the power coefficient is shown. The maximum value of the power coefficient is about 0.194 for $\delta = 0.15$, and 0.223 for $\delta = 0.0$. Accordingly, this observation motivated the authors to study the effect of the overlap ratio on rotor performance with an optimum twist angle of $\varphi = 45^\circ$ as will be discussed in the following subsection.

To further explore the performance enhancement achieved by using

a twisted Savonius rotor with a twist angle of $\varphi = 45^\circ$, the variation of C_T during a complete revolution, and the pressure distribution are presented and compared with the Savonius rotor with a twist angle of zero, and 180°. Fig. 13 illustrates the variation of instantaneous torque coefficient with the rotation angle θ ranged from 0° to 360° for the advancing blade, the returning blade, and the whole rotor at $\lambda = 0.8$, $\delta = 0.15$, and $V = 6$ m/s. Based on the figure, at a twist angle of 45°, the highest average C_T of both returning and advancing blades is achieved and then, the whole rotor is compared with a twist angle of 0° and 180°. Despite, having the lowest average value of C_T with a rotor twist angle of 180°, the variation in the C_T within the whole cycle is smoother than those of alternative twist angles. The smooth variation in the C_T s is very useful in reducing mechanical vibrations.

Fig. 14 shows the pressure distribution along with streamlines at $\lambda = 0.8$ and a rotor angle of $\theta = 0^\circ$ at different sections across the rotor height, and different twist angles of $\varphi = 0^\circ$, 45° , and 180° . For the untwisted rotor, $\varphi = 0^\circ$, the pressure distribution was almost the same for all sections as the blades are straight except for a small deviation caused by the endplates. In addition, the air pressure is the maximum at the tip of the advancing blade at all sections and reduces with further movement along the convex surface. This will cause flow separation at

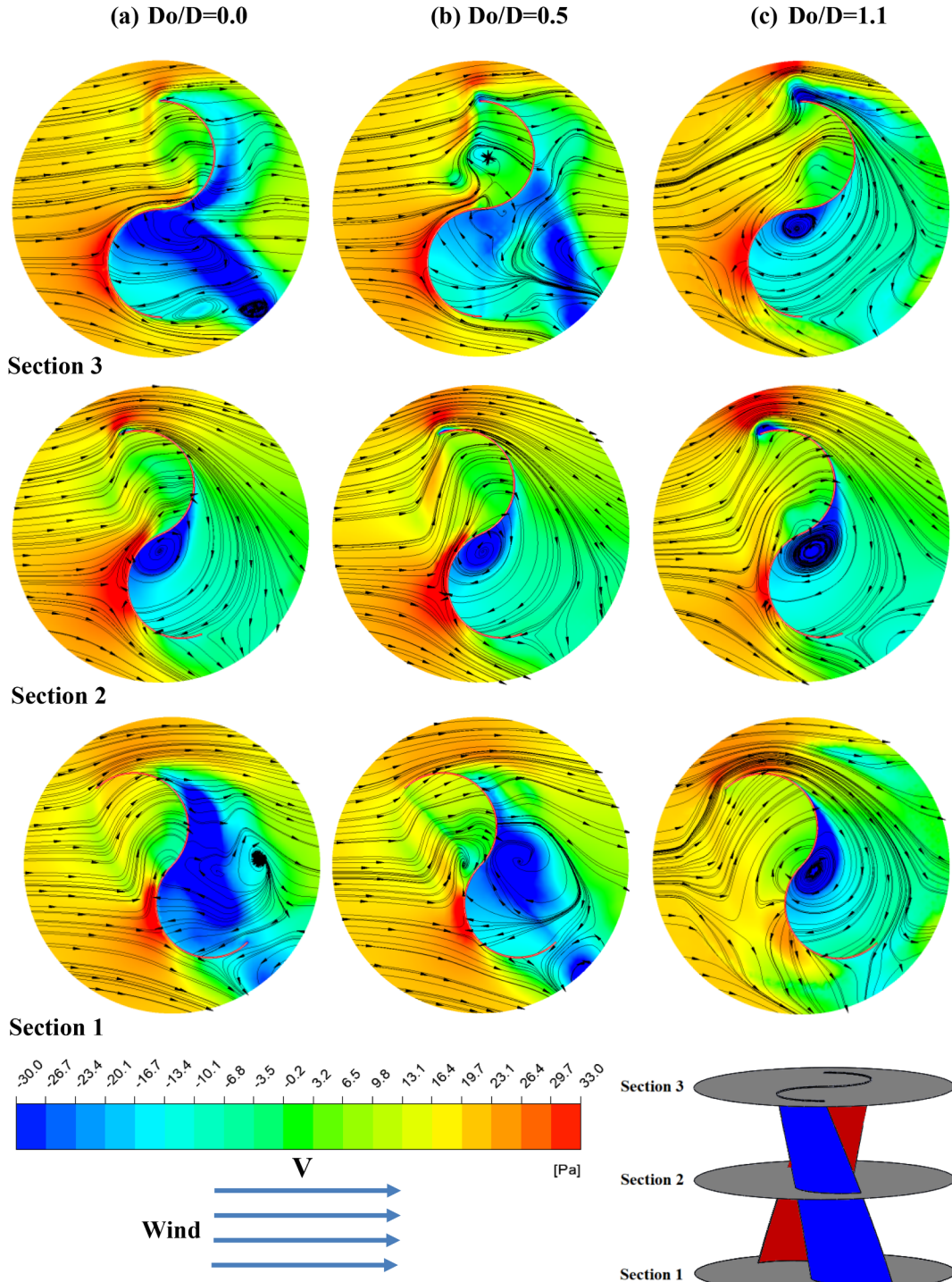


Fig. 20. Sectional total pressure distribution around the blades at rotor angle $\theta = 45^\circ$ for (a) $Do/D = 0.0$, (b) $Do/D = 0.5$, (c) $Do/D = 1.1$.

the end of the advancing blade due to adverse pressure gradients. This trend is observed for all cases shown in Fig. 14, except at section-2 in the case of $\varphi = 180^\circ$ due to the vertical position of the advancing blade. At a twist angle of 45° , it is observed that the pressure on the concave surface of the advancing blade is higher than those at both $\varphi = 0^\circ$ and 180° due to varying the blade twist angle. Moreover, the air mass flow rate hitting the concave surface of the advancing blade is much higher than that of both $\varphi = 0^\circ$ and 180° . Consequently, a significant increase of positive torque offered by the advancing blade is clearly observed in Fig. 13(a) at $\theta = 0^\circ$.

At $\varphi = 0^\circ$, the pressure distribution on the convex surface of the

returning blade is higher than that of the concave surface. Accordingly, a negative torque is required to drive the rotor. With further increase of twist angle up to 45° , the pressure distribution on the convex surface of returning blade increases, while the pressure on the concave surface almost remains constant. This will result in increasing the negative torque required to drive the rotor. At $\varphi = 180^\circ$, the pressure distribution is only high at section-2 and significantly decreases as shown in section-1, and section-3. Consequently, the negative torque required to drive the rotor is less than that at $\varphi = 45^\circ$. As a result, the negative torque generated by the returning blade at $\varphi = 180^\circ$ was a little higher than that at $\varphi = 0^\circ$ and marginally lower than that at $\varphi = 45^\circ$ as shown

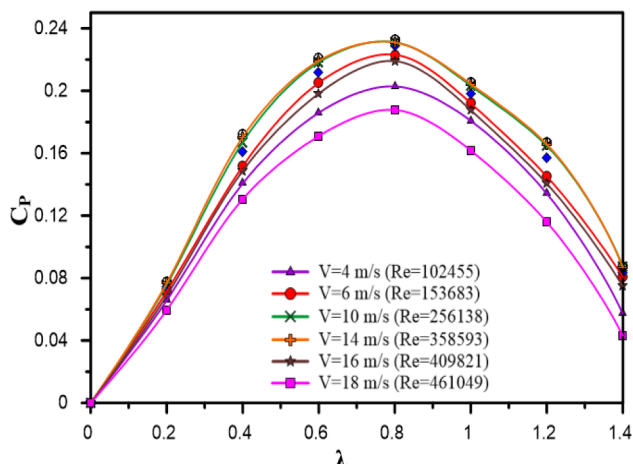


Fig. 21. The effect of the wind speed on the performance of the optimum design of the twisted Savonius rotor.

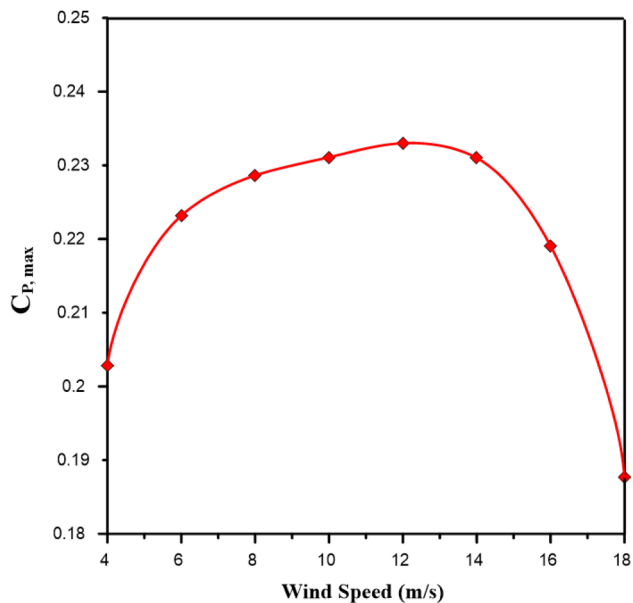


Fig. 22. The maximum power coefficient $C_{P,\max}$ of the optimum design of the twisted Savonius rotor at various wind speeds.

in Fig. 13(b). However, the percentage increase in positive torque was significantly higher than the percentage increase in negative torque for $\varphi = 45^\circ$ compared to $\varphi = 0^\circ$, and 180° . This leads to a high average C_T of the rotor at $\varphi = 45^\circ$ as compared with $\varphi = 0^\circ$ and 180° , as shown in Fig. 13(c). It is worth mentioning that the upper part of the twisted rotor at $\varphi = 45^\circ$ has a great share in the increase of that rotor C_T . The sharp change in the orientation of sections at $\varphi = 180^\circ$ significantly decreases the positive torque generated by its advancing blade which leads to decrease the performance.

5.2. Effect of overlap ratio

The variations of the predicted torque and power coefficient with a tip speed ratio for various overlap ratios (δ) at a wind speed of 6 m/s, and twist angle of 45° are presented in Fig. 15-a, and b, respectively. As seen in the figure, the torque and power coefficients significantly decrease as the overlap ratio increases from 0 to 0.35. At an overlapping ratio of zero, the values of C_T and C_P are 0.38 and 0.223, respectively. Here, it is worth mentioning that for the conventional rotor ($\varphi = 0^\circ$), the highest values of C_T and C_P were observed at $\delta = 0.15\text{--}0.2$.

To further explore the performance enhancement achieved by the twisted Savonius rotor ($\varphi = 45^\circ$) without overlapping ($\delta = 0.0$), the variation of C_T within a complete revolution and pressure distribution with streamlines were presented in Figs. 16 and 17, respectively. Fig. 16 shows the variation of the torque coefficient with rotation angle θ for the advancing blade, the returning blade, and the whole rotor. The torque coefficient was calculated during a complete cycle, from $\theta = 0$ to 360° , at $\lambda = 0.8$ and $V = 6$ m/s for the twisted Savonius rotor ($\varphi = 45^\circ$) at overlap ratios of 0.0, 0.15, and 0.3. The rotor without overlapping ($\delta = 0.0$) shows the highest C_T by the whole rotor blades at all rotor angles except a small range of rotor angles between $\theta = 60^\circ$ to 120° and $\theta = 240^\circ$ to 300° , as compared with $\delta = 0.15$ and 0.3. The rotor with $\delta = 0.3$ showed the lowest average C_T by both returning and advancing blades and in return by the whole rotor over a complete cycle.

Fig. 17 presents the local pressure distribution at three different sections across the rotor at an angle of $\theta = 0^\circ$. At the tip of the advancing blade, the air pressure is high and decreases as the air travels along the convex surface of the advancing blade. Due to the adverse pressure gradient, the flow separates from the surface and creates a highly turbulent region behind the advancing blade. Due to flow separation and recirculating flow, the wake zone appears in the flow domain behind the advancing blade. The pressure inside the wake region remains low as the flow separates, and a net pressure force (positive drag) is produced. For a rotor without overlap at $\delta = 0.0$, it was observed that the total pressure at the concave surface of the advancing blade was higher than that of the overlapped rotors ($\delta = 0.15$ and 0.3) which increased the positive torque generated by the advancing blade which was also clearly observed from previous Fig. 16(a) at $\theta = 0^\circ$. This was due to flow escaping the overlap region at $\delta = 0.15$ and 0.3 which decreased the pressure while there is no escaped flow for the rotor without overlap. Moreover, the recirculating flow in front of the overlap region at $\delta = 0.0$ acted as a jet which increased the momentum of the oncoming flow which in turn increased the total pressure. Furthermore, the lower part of the advancing blade at $\delta = 0.15$ and 0.3 was not directly facing the oncoming flow and in return decreases the positive torque generated by the advancing blade. However, the negative torque generated by the returning blade of the rotor without overlap was slightly higher than that of the overlapped rotors ($\delta = 0.15$ and 0.3) which can be found in Fig. 16 (b) at $\theta = 0^\circ$. This was due to the recirculating flow behind the overlap region for a rotor with $\delta = 0.0$ at very low pressure which decreases the pressure on the concave surface of the returning blade and in return increases the negative torque. Moreover, the recirculating flows behind the overlap region for a rotor with $\delta = 0.0$ act as a shield and prevent some flow from hitting the concave surface of the returning blade. However, the percentage increase in positive torque is higher than the percentage increase in negative torque for the rotor without overlap compared to overlapped rotors ($\delta = 0.15$ and 0.3). This leads to a high average C_T of the whole blades at $\delta = 0.0$ as compared to $\delta = 0.15$ and 0.3 at a rotor angle of 0° , as shown in Fig. 16 (c).

5.3. Effect of endplates size ratio

The variation of the torque and power coefficients with tip speed ratio for various sizes of endplates at a wind speed of 6 m/s are presented in Fig. 18-a and b, respectively. It is found that using endplates significantly increases the power coefficient of the twisted Savonius rotor. Based on the figures the torque coefficient increases with an increase in the endplates size ratio from zero to 1.1. With a further increase beyond 1.1, a reduction of both torque and power coefficient is observed. The reason is likely due to the endplates preventing the escape of air from the tips of the concave side of both the advancing and returning blades to the external domain. This keeps the pressure difference between the concave and convex side of the blades at high levels over the height of the turbine.

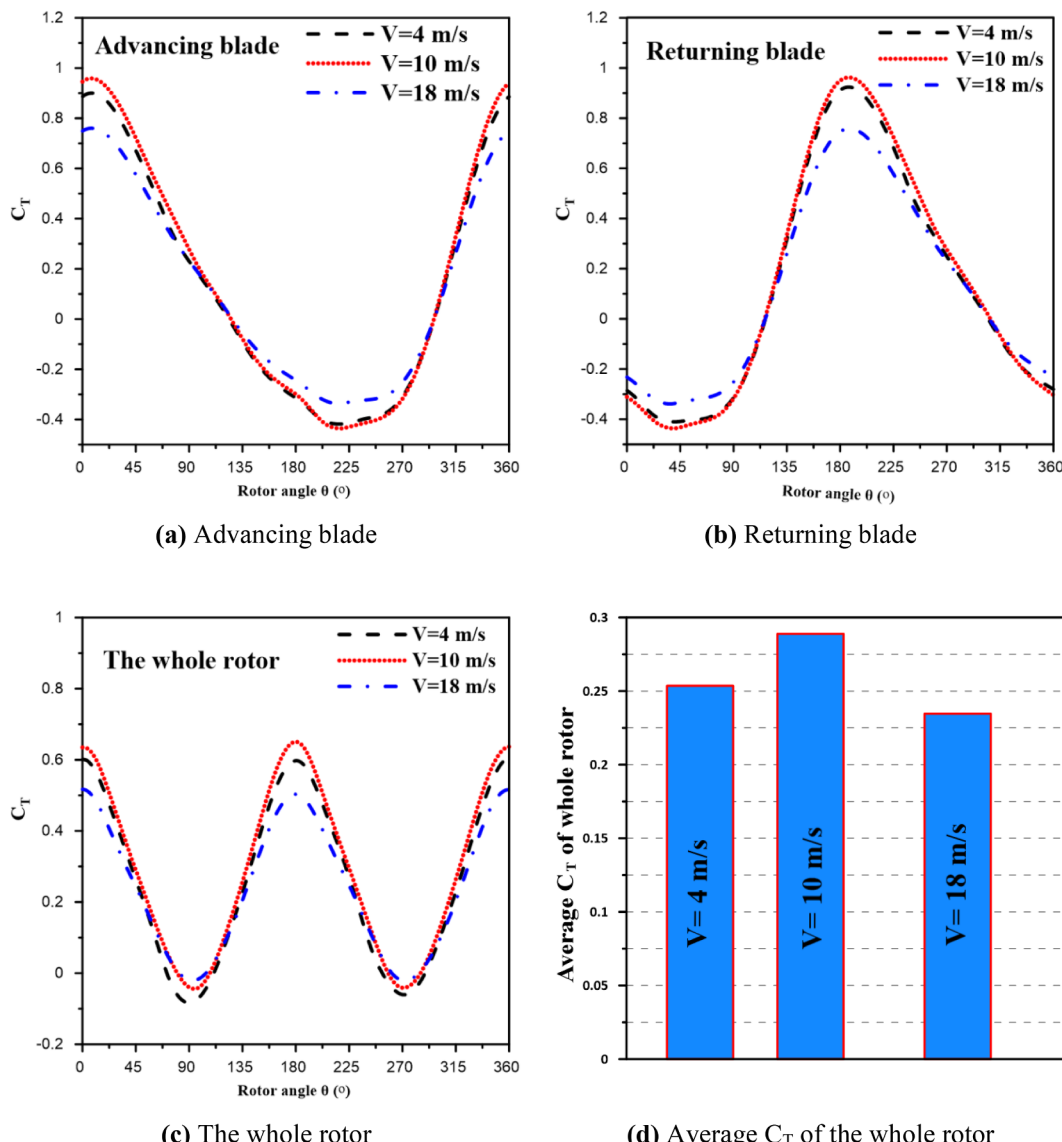


Fig. 23. Instantaneous torque coefficient versus rotor angle over complete revolution for (a) Advancing blade (b) Returning blade (c) The whole rotor, and (d) Average torque coefficient of the whole rotor.

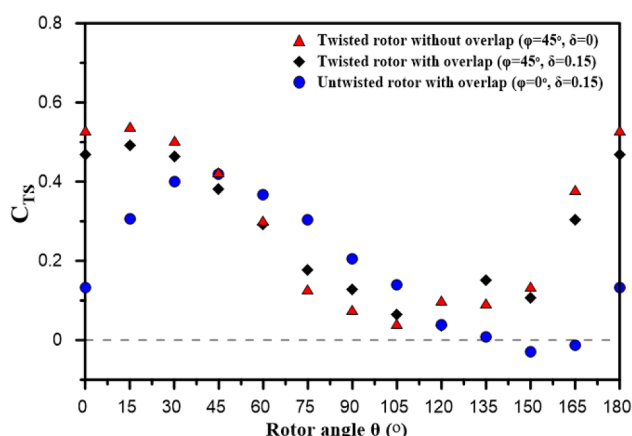


Fig. 24. Static torque coefficient obtained numerically versus rotor angle of the studied Savonius rotors.

To further analyze the performance enhancements achieved by the twisted Savonius rotor with an optimum size of endplates ($Do/D = 1.1$), the C_T during a complete revolution and pressure distribution with streamlines are presented at $\varphi = 45^\circ$, $\lambda = 0.8$ and $V = 6$ m/s. Fig. 19 shows the variation of the torque coefficient with rotation angle θ for the advancing blade, the returning blade, and the whole rotor. The torque coefficient was calculated within a complete cycle, from $\theta = 0$ to 360° for twisted Savonius rotor with endplates sizes $Do/D = 0.0$, $Do/D = 0.5$, and $Do/D = 1.1$. The rotor with endplate size $Do/D = 1.1$ showed higher C_T by the whole rotor blades at all rotor angles except a small range of rotor angles between $\theta = 100$ to 160° and $\theta = 280$ to 340° , compared to $Do/D = 0.0$, $Do/D = 0.5$. Therefore, the torque coefficient of the whole rotor within the complete cycle shows the highest average torque coefficient for the rotor with endplate size $Do/D = 1.1$. The rotor without endplates ($Do/D = 0.0$), showed the lowest average C_T in both returning and advancing blades and in return by the whole rotor over the complete cycle.

Fig. 20 presents the total pressure distribution at three different sections across the rotor. For advancing blades at all rotors, it was observed that the pressure distribution at both concave and convex surfaces was almost the same at all sections generating approximately

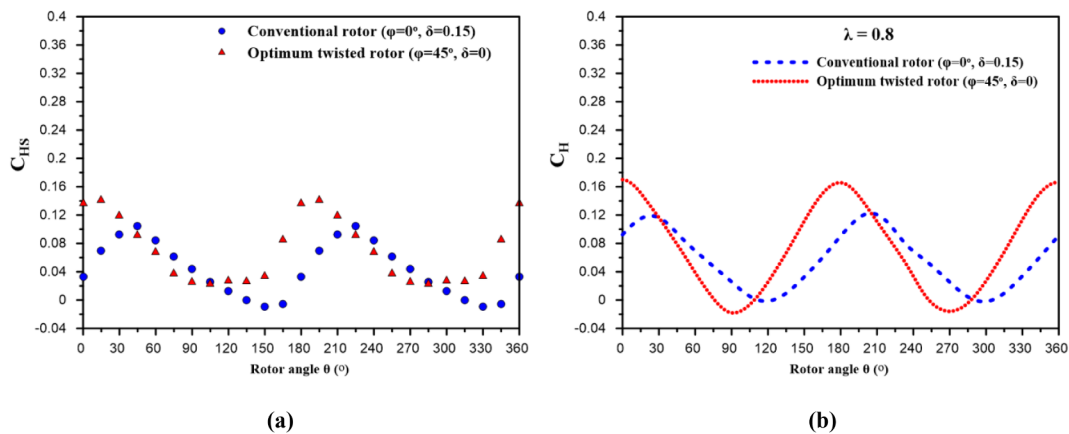


Fig. 25. (a) Static thrust coefficient and (b) dynamic thrust coefficient versus rotor angle on the conventional and optimum twisted rotors.

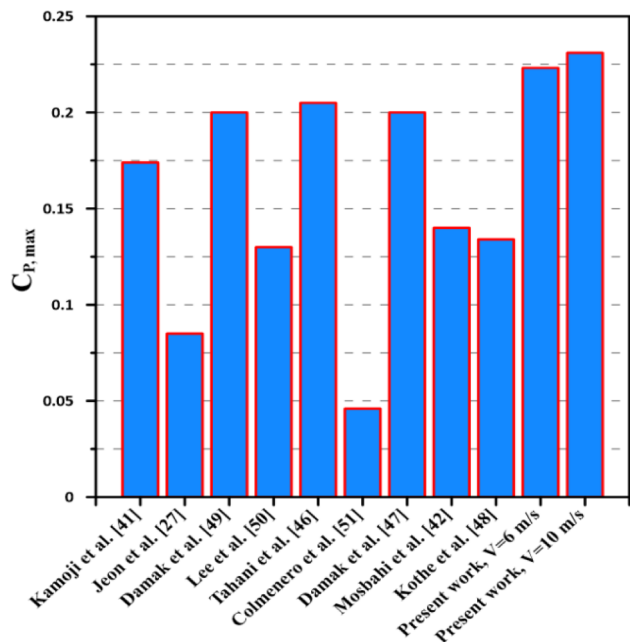


Fig. 26. Comparison of maximum power coefficient obtained by the present work and twisted rotors in the literature [27,41,42,46–51].

the same value of positive torque for all rotors which is seen in Fig. 19(a) at $\theta = 45^\circ$. However, the negative torque generated by the returning blade of the rotor without endplates was significantly higher than that of the rotors with $Do/D = 0.5$ and $Do/D = 1.1$. This was due to the pressure on the convex surface of the returning blade for $Do/D = 0.0$ was higher than that of $Do/D = 1.1$ at all sections. This is due to the oncoming flow directly impacts on the concave surface for $Do/D = 0.0$. However, for $Do/D = 1.1$, the oncoming flow separates before hitting the convex surface, due to the endplates, which leads to a decrease in negative torque. Moreover, the total pressure on the concave surface of the returning blade for $Do/D = 0.0$ was significantly lower than that of $Do/D = 1.1$ at all sections especially at tip sections 1 and 3 due to endplates effect.

Despite a similar generated positive torque at all rotors, the negative torque for the rotor with endplates $Do/D = 1.1$ was significantly lower than that of a rotor without endplates $Do/D = 0.0$ and a rotor with endplates $Do/D = 0.5$. This leads to the highest average C_T of the whole blades of $Do/D = 1.1$ as compared to other cases. It is worth mentioning that the lower and upper parts of the twisted Savonius rotor, due to endplates, increase the C_T of the rotor.

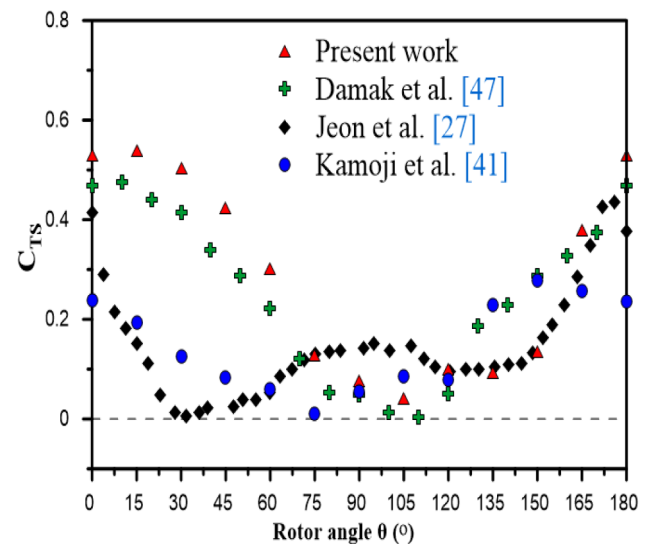


Fig. 27. Comparison of static torque coefficient obtained by the present work and twisted rotors in the literature [41,27,47].

5.4. Effect of wind velocity

The effect of wind velocity (V) on the performance of the best design of the twisted Savonius rotor is presented. The best design has a twist angle $\varphi = 45^\circ$, an overlap ratio $\delta = 0.0$, and endplate size $Do/D = 1.1$. These parameters are based on the best conditions extracted from the results discussed in the previous subsections.

Fig. 21 illustrates the variation in power coefficient of the rotor versus tip speed ratio at wind speed values (V) ranging from 4 to 18 m/s (corresponding to $Re = 102455$ to 461049) with a step increase of 2 m/s. It is observed that the power coefficient of the rotor increases with the rise of the inflow wind velocity at a range of $V = 4$ to 10 m/s. With a further increase of the wind velocity, there is no significant effect on the rotor performance. However, an increase in the wind speed beyond 14 m/s has a negative effect on the rotor performance. The values of the maximum power coefficient ($C_{P,max}$) at each wind velocity is presented in Fig. 22.

To investigate the performance enhancements achieved by the twisted Savonius rotor at wind velocity range of $V = 10$ to 14 m/s in which the performance was the highest, the C_T within a complete revolution is presented at $V = 10$ m/s and compared with the wind velocity at $V = 4$ m/s and $V = 18$ m/s. Fig. 23 shows the variation of the instantaneous torque coefficient with rotation angle θ for the advancing blade, the returning blade, and the whole rotor. The torque coefficient

Table 2

Comparison with previous research work.

Reference	Methodology	Blade profile	Twist angle	$C_{P,\max}$	λ at $C_{P,\max}$	Re	δ	AR
Kamoji et al. [41]	Experimental	Semi-circular	90°	0.174	0.65	15×10^4	0	0.88
Jeon et al. [27]	Experimental	Semi-circular	180°	0.085	0.58	13.8×10^4	0	2
Damak et al. [49]	Experimental	Semi-circular	180°	0.2	0.33	11.6×10^4	0.242	1.57
Lee et al. [50]	Numerical and experimental	Semi-circular	45°	0.13	0.54	1.55×10^6	0.167	1.33
Tahani et al. [46]	Numerical	Semi-circular	30°	0.205	0.7	8.84×10^4	0.2	1
Colmenero et al. [51]	Numerical and experimental	Semi-circular	45°	0.046	0.335	13.6×10^4	0.32	1.6
Damak et al. [47]	Numerical and experimental	Modified profile (Bach rotor)	90°	0.2	0.75	12.1×10^4	0	0.7
Mosbah et al. [42]	Numerical and experimental	semi-circular with deflector system	90°	0.14	0.7	15.6×10^4	0	0.88
Kothe et al. [48]	Numerical and experimental	Semi-circular	180°	0.134	0.65	4.63×10^3	0.15	4
Current work	Numerical	Semi-circular	45°	0.223	0.8	15.4×10^4	0	1
Current work	Numerical	Semi-circular	45°	0.232	0.8	25.6×10^4	0	1

was calculated within a complete cycle, from $\theta = 0$ to 360° , at $\lambda = 0.8$. At $V = 10$ m/s, the rotor attains higher C_T by the whole rotor at all rotor angles except a small range of rotor angles between $\theta = 75$ to 120° and $\theta = 255$ to 300° , as compared with $V = 4$ and 18 m/s. Therefore, the whole rotor during a complete cycle achieves the highest average value at $V = 10$ m/s. However, the rotor at $V = 18$ m/s shows the lowest average C_T by both returning and advancing blades and by the whole rotor over the complete cycle.

5.5. The self-starting ability of the rotor

Fig. 24 illustrates the static torque coefficient (C_{TS}) of the conventional untwisted rotor ($\varphi = 0^\circ$) with overlap ($\delta = 0.15$), and the twisted rotor ($\varphi = 45^\circ$) with two overlapping ratios of $\delta = 0$, and $\delta = 0.15$ at a wind speed of a 6 m/s. It was observed that twisted rotors always have positive C_{TS} values at all rotor angles. On the contrary, the untwisted rotor has a negative value at rotor angles of $\theta = 138^\circ$ – 167° . Hence, the twisted blades enhance the self-starting ability of the Savonius rotor. Using a twisted rotor without overlap attains the highest average C_{TS} compared to other studied rotors. Accordingly, the newly twisted rotor design not only enhances the power coefficient but the self-starting ability as well.

5.6. Thrust load on the rotor

Fig. 25 presents the static thrust coefficient (C_{HS}) and the dynamic thrust coefficient (C_H) at a tip speed ratio of 0.8. This is in the case of using a conventional untwisted rotor with $\varphi = 0^\circ$ and $\delta = 0.15$ and a twisted rotor with $\varphi = 45^\circ$ and $\delta = 0$ where the wind speed is kept at 6 m/s. From Fig. 25, it is obvious that both static and dynamic thrust coefficients vary periodically for every 180° , as the studied rotors are two-bladed. The optimum twisted rotor shows a slightly higher average of C_{HS} and C_H of 0.07 and 0.073, respectively over a complete cycle compared to 0.05 and 0.056 for the conventional rotor. The optimum twisted rotor benefits from the high-power coefficient and the self-starting capabilities, but it has a slightly higher thrust load on the rotor.

6. Comparison with previous work

The results obtained for the current twisted Savonius rotor present optimal design conditions such that $\varphi = 45^\circ$, $\delta = 0$, $Do/D = 1.1$, and $V = 6$ – 10 m/s are compared to available results reported in the literature as shown in Fig. 26. The comparison indicates that the present design attains the highest $C_{P,\max}$ of 0.223, and 0.231 at $V = 6$, and 10 m/s, respectively compared with other designs. Furthermore, Fig. 27 shows the comparison between the values of C_{TS} obtained by the present design and the available reported results of Kamoji et al. [41], Jeon et al. [27], and Damak et al. [47]. It is found that the current designs have positive C_{TS} at all rotor angles. However, other designs have low values of C_{TS} and approach zero values at specific rotor angles. Consequently, the current design achieves a high self-starting ability.

Table 2 provides details of the operating conditions of previously conducted work.

7. Conclusion

The effects of several design parameters including twist angle, overlap ratio, and endplates size ratio, along with the wind velocity on the performance of Savonius wind turbine are investigated. To assess the effect of the proposed designs on the wind turbine performance, a three-dimensional incompressible unsteady Reynolds-averaged Navier-Stokes model in conjunction with $k-\omega$ shear-stress transport (SST) turbulence model is developed. In light of current results, important findings are derived. Predicting the flow field around the Savonius rotor wind turbine is essential to understand the influence of design parameters. The Savonius rotor with a twist angle of 45° , an overlapping ratio of zero, and endplates size ratio of 1.1 attains the highest net output power compared with other designs. At wind velocity of 6 m/s, the Savonius rotor achieves the maximum power coefficient of 0.223, and with a further increase of the wind velocity to 10 m/s, the power coefficient reaches 0.231. Increasing the overlapping ratio of the Savonius rotor above zero creates eddies and vortices that cause a significant loss of flow kinetic energy. In addition, at a twist angle of 45° , more flow directly impacts on the concave surface of advancing and returning blades and increases total pressure, hence increasing the net torque generated by rotor compared to other angles. The upper and lower plates prevent the escape of air from concave side tips of advancing and returning blades. This will keep a pressure difference between the concave and convex sides of blades at high levels over the height of the turbine and accordingly enhances the energy conversion process. The endplates force the flow to leave the advancing blade with high momentum to impact on the concave surface of the returning blade causing a decrease in the negative torque and in return increases the net output energy. The newly twisted rotor design not only enhances the power coefficient but the self-starting ability as well. However, it has slightly higher thrust load. The current results provide a new direction for researchers and designers to utilize the twisted Savonius wind turbine

CRediT authorship contribution statement

Ahmed S. Saad: Conceptualization, Methodology, Writing - original draft, Software, Investigation. **Ibrahim I. El-Sharkawy:** Supervision, Writing - review & editing. **Shinichi Ookawara:** Supervision, Writing - review & editing. **Mahmoud Ahmed:** Conceptualization, Supervision, Writing - review & editing, Investigation, Methodology.

Declaration of Competing Interest

The authors declare that they have no known competing financial interests or personal relationships that could have appeared to influence the work reported in this paper.

Acknowledgement

Sincere gratitude and appreciation for the Egyptian Ministry of Higher Education (MOHE) as well as the Egypt-Japan University of Science and Technology (E-JUST) for offering the financial support and computational tools to conduct this research.

References

- [1] Edelenbosch OY, Kermeli K, Crijns-Graus W, et al. Comparing projections of industrial energy demand and greenhouse gas emissions in long-term energy models. *Energy* 2017;122:701–10.
- [2] Bonalumi D, Giuffrida A. Investigations of an air-blown integrated gasification combined cycle fired with high-sulphur coal with post-combustion carbon capture by aqueous ammonia. *Energy* 2016;117:439–49.
- [3] Yannopoulos SI, Lyberatos G, Theodossiou N, et al. Evolution of water lifting devices (Pumps) over the centuries worldwide. *Water (Switzerland)* 2015;7(9):5031–60.
- [4] Global Wind Energy Council (GWEC) Global Wind Energy Report 2018; April 2019.
- [5] Wang Y, Sun X, Dong X, Zhu B, Huang D, Zheng Z. Numerical investigation on aerodynamic performance of a novel vertical axis wind turbine with adaptive blades. *Energy Convers Manag* 2016;108:275–86.
- [6] Sharma S, Sharma RK. CFD investigation to quantify the effect of layered multiple miniature blades on the performance of Savonius rotor. *Energy Convers Manag* 2017;144:275–85.
- [7] Bianchini A, Ferrara G, Ferrari L. Design guidelines for H-Darrieus wind turbines: optimization of the annual energy yield. *Energy Convers Manag* 2015;89:690–707.
- [8] Rezaeih A, Kalkman I, Blocken B. Effect of pitch angle on power performance and aerodynamics of a vertical axis wind turbine. *Appl Energy* 2017;197:132–50.
- [9] Zhao D, Han N. Optimizing overall energy harvesting performances of miniature Savonius-like wind harvesters. *Energy Convers Manag* 2018;178(October):311–21.
- [10] Chen WH, Chen CY, Huang CY, Hwang CJ. Power output analysis and optimization of two straight-bladed vertical-axis wind turbines. *Appl Energy* 2017;185:223–32.
- [11] Goodarzi M, Keimanesh R. Numerical analysis on overall performance of Savonius turbines adjacent to a natural draft cooling tower. *Energy Convers Manag* 2015;99:41–9.
- [12] Eriksson S, Bernhoff H, Leijon M. Evaluation of different turbine concepts for wind power. *Renew Sustain Energy Rev* 2008;12(5):1419–34.
- [13] Toja-Silva F, Colmenar-Santos A, Castro-Gil M. Urban wind energy exploitation systems: behaviour under multidirectional flow conditions - Opportunities and challenges. *Renew Sustain Energy Rev* 2013;24:364–78.
- [14] Modi VJ, Fernando MSUK. Unsteady aerodynamics and wake of the savonius wind turbine: A numerical study. *J Wind Eng Ind Aerodyn* 1993;46–47:811–6. [https://doi.org/10.1016/0167-6105\(93\)90357-T](https://doi.org/10.1016/0167-6105(93)90357-T).
- [15] Sheldahl RE, Feltz LV, Blackwell BF. Wind tunnel performance data for two- and three-bucket Savonius rotors. *Energy* 1978;2(3):160–4.
- [16] Ferrari G, Federici D, Schito P, Inzoli F, Mereu R. CFD study of Savonius wind turbine: 3D model validation and parametric analysis. *Renewable Energy* 2017;105:722–34.
- [17] Bhayo BA, Al-Kayiem HH. Experimental characterization and comparison of performance parameters of S-rotors for standalone wind power system. *Energy* 2017;138:752–63.
- [18] Zhao Z, Zheng Y, Xu X, Liu W, Hu G. Research on the Improvement of the Performance of Savonius Rotor Based on Numerical Study. In the proceedings of international conference on sustainable power generation and supply (SUPERGEN). 2009: p. 1–6.
- [19] Kianifar A, Anbarsooz M. Blade curve influences on the performance of Savonius rotors: experimental and numerical. *Proc Inst Mech Eng, Part A: J Power Energy* 2011;225(3):343–50. <https://doi.org/10.1177/2041296710394413>.
- [20] Fujisawa N. On the torque mechanism of Savonius rotors. *J Wind Eng Ind Aerodyn* 1992;40(3):277–92.
- [21] Akwa JV, Da Silva Alves, Júnior G, Petry AP. Discussion on the verification of the overlap ratio influence on performance coefficients of a Savonius wind rotor using computational fluid dynamics. *Renew Energy* 2012;38(1):141–9.
- [22] C. Jian J. Kumbernuss Z. Linhua L. Lin Hongxing Y. Influence of phase-shift and overlap ratio on Savonius wind turbine's performance Journal of solar energy engineering. Feb 2012 1;134(1).
- [23] Saha UK, Thotla S, Maity D. Optimum design configuration of Savonius rotor through wind tunnel experiments. *J Wind Eng Ind Aerodyn* 2008;96(8–9):1359–75.
- [24] Emmanuel B, Jun W. Numerical study of a six-bladed Savonius wind turbine. *J Sol Energy Eng* 2011;133(4).
- [25] Mahmoud NH, El-Haroun AA, Wahba E, Nasef MH. An experimental study on improvement of Savonius rotor performance. *Alexandria Eng J* 2012;51(1):19–25.
- [26] Akwa JV, Vielmo HA, Petry AP. A review on the performance of Savonius wind turbines. *Renew Sustain Energy Rev* 2012;16(5):3054–64.
- [27] Jeon KS, Jeong Ji, Pan JK, Ryu KW. Effects of end plates with various shapes and sizes on helical Savonius wind turbines. *Renew Energy* 2015;79(1):167–76.
- [28] Kamoji MA, Kedare SB, Prabhu SV. Experimental investigations on single stage modified Savonius rotor. *Appl Energy* 2009;86(7–8):1064–73.
- [29] Hayashi T, Li Y, Hara Y. Wind tunnel tests on a different phase three-stage Savonius rotor. *JSME Int J Ser B* 2005;48(1):9–16.
- [30] Kamoji MA, Kedare SB, Prabhu SV. Experimental investigations on single stage, two stage and three stage conventional Savonius rotor. *Int J Energy Res* 2008;32:877–95.
- [31] Alom N, Saha UK. Influence of blade profiles on Savonius rotor performance: numerical simulation and experimental validation. *Energy Convers Manag* 2019;186:267–77.
- [32] Frikha S, Driss Z, Ayadi E, Masmoudi Z, Abid MS. Numerical and experimental characterization of multi-stage Savonius rotors. *Energy* 2016;114:382–404.
- [33] Mohan Kumar P, Surya MM, Narasimalu S, Lim TC. Experimental and numerical investigation of novel Savonius wind turbine. *Wind Eng* 2019;43(3):247–62.
- [34] Shojaeebad MH, Tahani M, Ehghaghi MB, Fallahian MA, Beglari M. Numerical study of the effects of some geometric characteristics of a centrifugal pump impeller that pumps a viscous fluid. *Comput Fluids* 2012;60:61–70.
- [35] Menter F. Two-Equation Eddy-Viscosity Turbulence Models for Engineering Applications. *AIAA Journal*. 1994;32(8):1598–605.
- [36] Plourde BD, Abraham JP, Mowry GS, Minkowycz WJ. Simulations of three-dimensional vertical-axis turbines for communications applications. *Wind Eng* 2012;36(4):443–53.
- [37] Fertahi S, Bouhal T, Rajad O, et al. CFD performance enhancement of a low cut-in speed current Vertical Tidal Turbine through the nested hybridization of Savonius and Darrieus. *Energy Convers Manag* 2018;169(May):266–78.
- [38] Wong KH, Chong WT, Sukiman NL, et al. Experimental and simulation investigation into the effects of a flat plate deflector on vertical axis wind turbine. *Energy Convers Manag* December 2017;2018(160):109–25.
- [39] Tian W, Mao Z, Ding H. Numerical study of a passive-pitch shield for the efficiency improvement of vertical axis wind turbines. *Energy Convers Manag* 2019;183:732–45.
- [40] Ostos I, Ruiz I, Gajic M, Gómez W, Bonilla A, Collazos C. A modified novel blade configuration proposal for a more efficient VAWT using CFD tools. *Energy Convers Manag* 2018;2019(180):733–46.
- [41] Kamoji MA, Kedare SB, Prabhu SV. Performance tests on helical Savonius rotors. *Renew Energy* 2009;34(3):521–9.
- [42] Mosbah M, Ayadi A, Chouaibi Y, Driss Z, Tucciarelli T. Performance study of a Helical Savonius hydrokinetic turbine with a new deflector system design. *Energy Convers Manag* 2019;194:55–74.
- [43] Fluent User's Guide Fluent 19.0. Fluent Incorporated, Lebanon, NH. 2019.
- [44] Tahani M, Babayan N, Mehrnia S, Shadmehr M. A novel heuristic method for optimization of straight blade vertical axis wind turbine. *Energy Convers Manag* 2016;127:461–76.
- [45] Orlandi A, Collu M, Zanforlin S, Shires A. 3D URANS analysis of a vertical axis wind turbine in skewed flows. *J Wind Eng Ind Aerodyn* 2015;147:77–84.
- [46] Tahani M, Rabbani A, Kasaeian A, Mehrpooya M, Mirhosseini M. Design and numerical investigation of Savonius wind turbine with discharge flow directing capability. *Energy* 2017;130:327–38.
- [47] Damak A, Driss Z, Abid MS. Optimization of the helical Savonius rotor through wind tunnel experiments. *J Wind Eng Ind Aerodyn* 2018;174:80–93.
- [48] Kothe LB, SéViç Möller, Petry AP. Numerical and experimental study of a helical Savonius wind turbine and a comparison with a two-stage Savonius turbine. *Renewable Energy* 2019.
- [49] Damak A, Driss Z, Abid MS. Experimental investigation of helical Savonius rotor with a twist of 180°. *Renew Energy* 2013;52:136–42.
- [50] Lee JH, Lee YT, Lim HC. Effect of twist angle on the performance of Savonius wind turbine. *Renewable Energy* 2016;1(89):231–44.
- [51] Mercado-Colmenero JM, Rubio-Paramio MA, Guerrero-Villar F, Martin-Doñate C. A numerical and experimental study of a new Savonius wind rotor adaptation based on product design requirements. *Energy Convers Manag* 2018;158:210–34.